

JGR Space Physics

RESEARCH ARTICLE

10.1029/2019JA027754

Key Points:

- Classification of jet database based on θ_{Bn} , using MMS data is presented
- All classes show different properties with some classes being compatible with existent generation mechanisms
- Bow shock ripple mechanism and SLAMS are generally supported by statistical properties

Supporting Information:

- Supporting Information S1
- Figure S1
- Data Set S1

Correspondence to:

S. Raptis,
savvra@kth.se

Citation:

Raptis, S., Karlsson, T., Plaschke, F., Kullen, A., & Lindqvist, P.-A. (2020). Classifying magnetosheath jets using MMS: Statistical properties. *Journal of Geophysical Research: Space Physics*, 125, e2019JA027754. <https://doi.org/10.1029/2019JA027754>

Received 20 DEC 2019

Accepted 13 OCT 2020

Accepted article online 16 OCT 2020

Classifying Magnetosheath Jets Using MMS: Statistical Properties

Savvas Raptis¹ , Tomas Karlsson¹ , Ferdinand Plaschke² , Anita Kullen¹ , and Per-Arne Lindqvist¹ 

¹Space and Plasma Physics, School of Electrical Engineering and Computer Science, KTH Royal Institute of Technology, Stockholm, Sweden, ²Space Research Institute, Austrian Academy of Sciences, Graz, Austria

Abstract Using Magnetospheric Multiscale (MMS) data, we find, classify, and analyze transient dynamic pressure enhancements in the magnetosheath (jets) from May 2015 to May 2019. A classification algorithm is presented, using in situ MMS data to classify jets ($N = 8,499$) into different categories according to their associated angle between interplanetary magnetic field (IMF) and the bow shock normal vector (θ_{Bn}). Jets appearing for $\theta_{Bn} < 45^\circ$ are referred to as quasi-parallel, while jets appearing for $\theta_{Bn} > 45^\circ$ as quasi-perpendicular jets. Furthermore, we define those jets that occur at the boundaries between quasi-parallel and quasi-perpendicular magnetosheath as boundary jets. Finally, encapsulated jets are jet-like structures with similar characteristics to quasi-parallel jets while the surrounding plasma is of quasi-perpendicular nature. We present the first statistical results of such a classification and provide comparative statistics for each class. Furthermore, we investigate correlations between jet quantities. Quasi-parallel jets have the highest dynamic pressure while occurring more often than quasi-perpendicular jets. The infrequent quasi-perpendicular jets have a much smaller duration, velocity, and density and are therefore relatively weaker. We conclude that quasi-parallel and boundary jets have similar properties and are unlikely to originate from different generation mechanisms. Regarding the encapsulated jets, we suggest that they are a special subset of quasi-parallel jets originating from the flanks of the bow shock, for large IMF cone angles although a relation to flux transfer events (FTEs) and magnetospheric plasma is also possible. Our results support existing generation theories, such as the bow shock ripple and SLAMS-associated mechanisms while indicating that other factors may contribute as well.

1. Introduction

The magnetosheath plasma can have strong fluctuations in velocity, density, and associated magnetic field. A key component that influences the level of fluctuation is the angle between the interplanetary magnetic field (IMF) and the bow shock normal vector (θ_{Bn}). It has been shown that in the case of the quasi-parallel shock ($\theta_{Bn} < 45^\circ$) the downstream plasma is strongly turbulent, whereas in the quasi-perpendicular shock ($\theta_{Bn} > 45^\circ$) there is a much smoother and calmer environment (Fuselier, 2013; Wilson III, 2016). The main reason the two regions have different characteristics is that in the quasi-parallel case, reflected ions can travel upstream along the magnetic field lines causing instabilities and associated wave growth. This creates a foreshock region characterized by a suprathermal ion distribution. This region is not present in the quasi-perpendicular case where the transition between upstream and downstream flow is distinct and straightforward (Schwartz & Burgess, 1991). As a result, in the quasi-perpendicular bow shock, there are much sharper and well-defined transitions between the upstream and downstream plasma.

Magnetosheath jets are local enhancements of dynamic pressure above the surrounding background level, reaching values even higher than the upstream solar wind. The dynamic pressure enhancements can be attributed to a density increase (Karlsson et al., 2012, 2015; Savin et al., 2008), a velocity increase (Archer et al., 2012), or may result from an enhancement of both (Amata et al., 2011; Plaschke et al., 2013). These jets are mainly found downstream of the quasi-parallel bow shock, and the current prominent formation theory is that they result from foreshock fluctuations interacting with the bow shock.

Many terms and definitions have been used in the literature to describe the jet phenomenon, as thoroughly discussed in the review paper by Plaschke et al. (2018). In principle, the jet determination can be done via two methods. The first one is by using a sliding average time window which indicates a background value on

©2020. The Authors.

This is an open access article under the terms of the Creative Commons Attribution License, which permits use, distribution and reproduction in any medium, provided the original work is properly cited.

the magnetosheath dynamic pressure and searches for enhancements that are 100–200% higher than that value. (Archer & Horbury, 2013; Gunell et al., 2014; Gutynska et al., 2015; Karlsson et al., 2015). Another way is to apply a minimum threshold to the x component of the dynamic pressure to be at least 25% of the solar wind's associated dynamic pressure (Amata et al., 2011; Hietala et al., 2012; Plaschke et al., 2013). In this work we will use the term “magnetosheath jet” or “jet” to describe an enhancement in the dynamic pressure compared to the values of the background magnetosheath plasma, using a sliding time window.

The dynamic pressure enhancements can reach up to ~15 times the background value. Their duration can be of the order of seconds, up to several minutes with an average of 30 s (Archer & Horbury, 2013). Parallel to the flow, the scale is $\sim 0.5 R_E$ and in the perpendicular direction slightly more at roughly $\sim 1 R_E$ (Archer & Horbury, 2013; Plaschke et al., 2018). While as mentioned above, jets' dynamic pressure enhancement is usually attributed to both density and velocity increase (Amata et al., 2011; Archer & Horbury, 2013), there are cases where some jets exhibit a density decrease. Specifically, Plaschke et al. (2013), found 10.5% of jets showing a density decrease. On the other hand, Archer et al. (2012) using a different jet criterion found up to 18% of jets exhibiting a density drop. Furthermore, jets can generate a vortical motion in the background magnetosheath plasma, causing a deceleration to the ambient plasma around the jet (Plaschke & Hietala, 2018). It has been recently shown that jets occur roughly 9 times more often downstream of the quasi-parallel bow shock compared to the quasi-perpendicular one (Vuorinen et al., 2019). This is in agreement with the observations showing low solar wind cone angles favoring the formation of subsolar magnetosheath jets, while other solar wind parameter variations have no significant effect (Plaschke et al., 2013).

Magnetosheath jets may have an important impact on the magnetosphere. Their increased momentum can create local deformation of the magnetopause and trigger local magnetic reconnection (Hietala et al., 2018), drive compressional waves (Plaschke & Glassmeier, 2011) or even cause direct plasma penetration in the magnetosphere (Dmitriev & Suvorova, 2015; Karlsson et al., 2012). Furthermore, they can affect the radiation belts through the loss of outer belt electrons, (Turner et al., 2012; Xiang et al., 2016). Additionally, jets can cause aurora brightening through the compression of the magnetosphere (Wang et al., 2018) or can affect the aurora via the mechanism of “dayside throat aurora” which has been connected to magnetosheath particle precipitation (Han et al., 2017). The link between jets and energy transfer through the magnetosphere was also observed recently when surface eigenmodes were found to be excited through a collision between a jet and the magnetopause (Archer et al., 2019). Finally, jets seem to be a universal phenomenon that is speculated to occur in other planetary and astrophysical bow shocks (Giacalone & Jokipii, 2007; Plaschke et al., 2018).

1.1. Generation of Jets

While the generation of jets is not yet fully explained, a prominent theory is that the majority of the jets are associated with ripples of the quasi-parallel bow shock. Hietala et al. (2009) and Hietala and Plaschke (2013) propose that through the interaction with a locally curved bow shock, plasma flows are less decelerated while still being compressed. This results in a relative velocity difference compared to the surrounding flow that gets more decelerated, explaining the dynamic pressure enhancement (“jet”) observed in the magnetosheath region. A similar mechanism, where foreshock short large-amplitude magnetic structures (SLAMS) interact with the local bow shock ripples may be responsible for generating some jets. SLAMS (upstream pulsations) are typical phenomena in the quasi-parallel foreshock and have very large magnetic field amplitudes (~ 5 times higher than the background) (Schwartz et al., 1992). Regarding jets, it has been suggested that jets associated with SLAMS can have a relative increase of density and magnetic field strength whereas the ones associated with purely bow shock ripple mechanism may be mainly velocity driven (Karlsson et al., 2015). Furthermore, there have been recent simulations supporting the generation of a SLAMS-like subset of jets (Palmroth et al., 2018).

Another theory associates the formation of jet-like transient phenomena with IMF rotational discontinuities. Early simulations have shown that pressure pulses may be generated when there is a switch between quasi-perpendicular and quasi-parallel bow shock or vice versa (Lin et al., 1996). Later, Dmitriev and Suvorova (2012) reported evidence of a jet, generated by a rotational discontinuity. Archer et al. (2012) found several jets that were consistent with this picture by using upstream and downstream solar wind data, while Karlsson et al. (2018) investigated the anatomy of some typical cases that exhibit a magnetic field rotation in the magnetosheath.

Additional mechanisms have been suggested, involving solar wind discontinuity-related hot flow anomalies (HFAs) which can act as an obstacle to the upstream solar wind flow (Savin et al., 2012). Another possible mechanism relates jets to the spontaneous hot flow anomalies (SHFAs) resulting from foreshock cavitons (Omidi et al., 2013; Zhang et al., 2013). Retinó et al. (2007) connected magnetic reconnection inside the magnetosheath with local particle acceleration which could appear as jets. This mechanism, however, is not sufficient to explain jets with velocities much greater than the local Alfvén speed (Archer et al., 2012). Other proposed mechanisms describe the jet phenomenon in terms of a slingshot effect (Chen et al., 1993; Lavraud et al., 2007). This effect attributes the velocity enhancement of jets to a release of magnetic tension of a flux tube along the flanks.

There is no consensus regarding which of the above theories is responsible for the origin of jets. Furthermore, there has been no investigation regarding statistical differences that may arise in the properties of the jets depending on the angle between the IMF field and the bow shock normal vector. In this work, we address both of these knowledge gaps by defining different classes of jets and investigating their statistical properties to give insight into how likely each generation mechanism is for each class.

1.2. Different Types of Jets

Using MMS data we identify and classify the jets into four main categories. Jets have been observed for over 20 years now downstream of the quasi-parallel bow shock (Němeček et al., 1998). It is believed that the majority of jets are occurring in a quasi-parallel configuration and therefore the first category we search for are the "Quasi-parallel (Qpar) jets." As a complementary category, we are investigating cases of jets that are downstream of the quasi-perpendicular bow shock that we call "Quasi-perpendicular (Qperp) jets." Furthermore, we classified jets that are found at the boundary between a Qpar and a Qperp geometry or vice versa. Our goal is to investigate if these jets are connected to the mechanism proposed by Archer et al. (2012), and we call them "Boundary jets." It has been hypothesized that maybe these jets are different than the other classes and may hold separate properties (Archer & Horbury, 2013; Archer et al., 2012; Karlsson et al., 2018). Finally, after inspecting the derived data set, we introduce a category called "Encapsulated jets." These jets contain plasma with very similar characteristics to Qpar, while the surrounding plasma is of Qperp nature.

Apart from the main categories, in the jet database, we include two more classes. The first are the ones that were identified as jets but were not classified by the algorithm by not fulfilling all necessary criteria. These jets, therefore, remain as "Unclassified jets" until further inspection. Second, jets found very close to either the bow shock or the magnetopause ("Border jets") are not investigated in this work to exclude possible edge effects. The main goal of this work is to investigate the statistical properties and the differences between these classes. As a result, the goal of the classification procedure is to derive enough samples to provide meaningful comparison and not to provide a class for every observed event. This was done in order to minimize misclassification and to only have very clear cases for each class.

2. Data

In this study, we use data starting from 1 September 2015 until 1 May 2019. For the measurements that characterize the jets in the magnetosheath, we use data from the MMS (Magnetospheric Multiscale) mission (Burch et al., 2016), while for the upstream values of the solar wind we use data primarily from the ACE (Advanced Composition Explorer) mission (Stone et al., 1998). The measurements used for both solar wind and magnetosheath regions are presented in Geocentric Solar Ecliptic (GSE) coordinates.

2.1. MMS—Magnetosheath Data

For magnetic field measurements, we use the fluxgate magnetometer (FGM) (Russell et al., 2016) which has a resolution of 1/0.125 sample/s in the slow survey mode. Furthermore, we use the fast plasma investigation (FPI) (Pollock et al., 2016) which has a time resolution of 4.5 s for ion measurements. Finally, for determining the position of MMS, the Magnetic Ephemeris Coordinates (MEC) data that are included in the MMS data set are used (Burch et al., 2016).

During their orbit, the MMS spacecraft are regularly traversing the magnetosheath region. The small separation of the four MMS spacecraft allows us to only use data from MMS1 for the purposes of this paper.

2.2. OMNIweb/ACE—Solar Wind Data

For parts of the analysis, we use upstream solar wind measurements, publicly available through the 1-min resolution OMNI database. This data set is created using multiple spacecraft measurements (primarily ACE and Wind Stone et al., 1998) and is smoothed and time shifted to the nose of the Earth's bow shock. The bow shock location changes according to the solar wind parameters and is automatically adjusted for every time-shifted measurement (King & Papitashvili, 2005). The time resolution of the OMNIweb high-resolution database is one data point per minute. To associate OMNIweb data to the jets we took average solar wind values of a 15-min window, starting 10 min before the jet's observation time and up to 5 min after. This value seemed to provide accurate results in the cases that we tested manually and was done to compensate for several possible errors that are explicitly analyzed in section 3 below. As a result, every jet that has been measured by MMS in the magnetosheath is associated to average solar wind quantities from the OMNIweb database.

3. Method

3.1. Magnetosheath Identification

The determination of each region (magnetosheath/solar wind/magnetosphere) is done based on manually derived thresholds for ion number density (n_i), velocity (V_i), temperature (T_i), and differential energy flux of high-energy ions (F_i). Furthermore, we require three (3) sequential data points to be classified as a different region in order to change the region's characterization (e.g., transitioning from the magnetosheath to the solar wind). This was done to avoid cases where due to the variance of the measurements, one point might be misclassified as another region. Finally, we impose a minimum duration for each region to be 15 min. Smaller regions were considered to be possibly influenced by bow shock or magnetopause crossings.

3.2. Jet Determination

For jet determination, we rely only on local magnetosheath data. Doing so, we increase the data set sample size by not limiting observations to time periods where upstream solar wind data are available. We found that roughly $\sim 27\%$ of the jets contained missing data in their corresponding solar wind dynamic pressure. As a result, the choice of local MMS measurements for jet determination appears to be superior regarding the size of the derived data set.

For the initial data set, we impose a minimum relative dynamic pressure threshold, which defines a jet as the time interval in which the dynamic pressure is at least twice as large as a 20-min average value. Specifically, we use:

$$P_{msh} \geq 2\langle P_{msh} \rangle_{20\text{ min}} \quad (1)$$

where,

$$P_{msh} = m_p n_i V_i^2 \quad (2)$$

and angular brackets denote an averaging by a 20 min sliding window. When magnetosheath regions are less than 20 min, the average window is taken to be equal to the available region. The choice of this criterion was primarily done to compare with other statistical works done with a similar criterion (e.g., Archer et al., 2012). Furthermore, criteria using solar wind values were avoided since the presented work contains jets occurring at the flanks of the magnetosheath, and such criteria would be met all the time.

We then implement an additional criterion, combining all the jets that have a shorter time separation than 60 s from each other.

$$t_{start,i+1} - t_{end,i} \geq 60 \text{ s} \quad (3)$$

Where $i = 1, 2, 3 \dots n$ is the number of the jet in the database.

This was done based on the assumption that jets with such a small time separation are part of the same fast plasma flow. A similar technique is also applied when studying flows that occur in the plasma sheet, known as bursty bulk flows (BBFs) (Angelopoulos et al., 1994). Furthermore, not combining jets may lead to skewed statistics since it can result in an artificially increased number of jets with much shorter duration and similar properties, possibly causing misleading results.

Table 1
Initial Data Set of the Magnetosheath Jets for the Period October 2015 to April 2019

Subset	Number (<i>n</i>)	Percentage (%)	Criteria
All	16,034	100	Equation 1
Combined	8,499	53	Equations 1 and 3

After obtaining the jet data set, as shown in Table 1, we implement an automatic classification algorithm to create a subset of jets for each class. The algorithm includes five stages of classification that are implemented sequentially. The purpose of this method is to increase the number of jets that are classified after every stage while only slightly increasing the misclassification cases. In the following subsections, we will briefly explain some key ideas and components of the algorithm, while more details can be found in Appendices A1 and B1 and in the supporting information.

3.3. Jet Classification

For the jet classification, we only use MMS data. Similar to the jet determination algorithm, the classification code avoids the use of solar wind measurements. This was done for several reasons. The solar wind values available are measured at L_1 and are time-lagged, introducing an error from the artificial propagation to the bow shock nose. The generated error in such a time-lagging procedure can reach values up to 30 min (Case & Wild, 2012; Mailyan et al., 2008), while producing large uncertainty in short time scale phenomena (e.g., rotations of magnetic field). Furthermore, the available measurements are averaged to 1 min, which makes certain short time scale features impossible to detect. Additionally, the jets are identified throughout the whole magnetosheath region, meaning that one has to time shift the associated solar wind values after the bow shock interaction, differently for each jet, in order to accurately characterize the jets, providing additional uncertainty to the measurements. Finally, for roughly one fourth of the jets IMF measurements were not available for a sufficiently long period of time to accurately classify them. All the above reasons led us to primarily use magnetosheath data rather than solar wind for the classification.

It has been shown that the quasi-parallel (Qpar) magnetosheath has different properties than the quasi-perpendicular (Qperp) magnetosheath. Specifically, in Qpar magnetosheath, temperature anisotropy is typically different compared to the Qperp one (Anderson et al., 1994; Fuselier et al., 1994). Furthermore, stronger fluctuations in the plasma density, velocity, and the magnetic field have been associated with Qpar magnetosheath (Formisano & Hedgecock, 1973; Luhmann et al., 1986). Finally, the most striking difference is a distinct high-energy ion population that can be observed in the Qpar magnetosheath (Fuselier, 2013; Gosling et al., 1978). Therefore, the classification code works by applying manually derived thresholds to the ion energy flux, temperature anisotropy, and magnetic field standard deviation. The quantities used for the classification are discussed later, while the values for each threshold are provided in Appendix A1.

The characteristics of the four main classes of jets are summarized in Table 2.

In order to verify that we can accurately distinguish between Qpar and Qperp magnetosheath, we checked the measurements of MMS when it was close to the subsolar point of the bow shock. Due to the proximity to the subsolar point, there is a smaller error in the propagation of the solar wind measurements to the bow shock, and a shorter distance for the plasma flow to propagate inside the magnetosheath. Therefore, we can

Table 2
Properties of the Four Main Classes of Jets

Name	Characteristic
Quasi-parallel	High-energy ion flux, low ion temperature anisotropy, high magnetic field variance
Quasi-perpendicular	Low-energy ion flux, high ion temperature anisotropy, low magnetic field variance
Boundary	Switch between Qpar characteristics to Qperp or vice versa
Encapsulated	Switch from Qperp characteristics to Qpar and back to Qperp

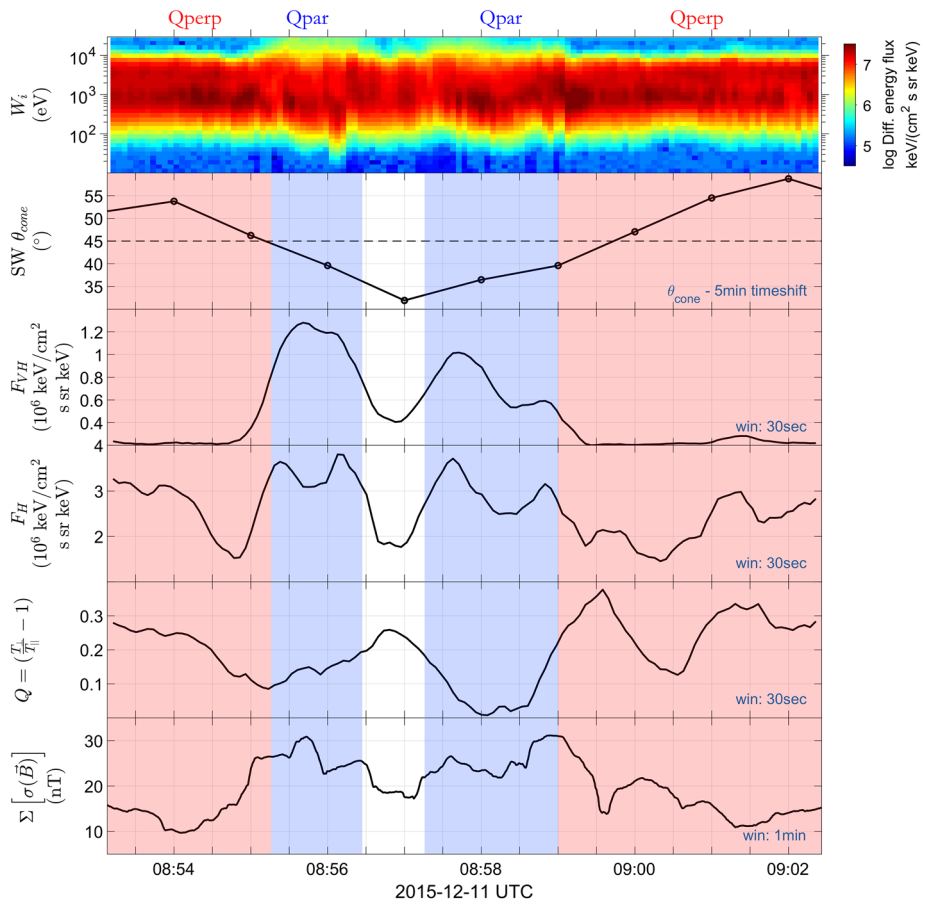


Figure 1. Visualization of associated changes between Qpar and Qperp magnetosheath. From top to bottom, ion energy spectrogram, solar wind cone angle, very high energy (16–28 keV) averaged differential ion flux, high-energy (7–12 keV) averaged differential ion flux, ion temperature anisotropy, and sum of the magnetic field standard deviation. Blue-shaded region represent Qpar regions while red show Qperp ones. More information about the computation of each quantity can be found in Appendix A1.

confirm the expected characteristics of the magnetosheath plasma. An example of such a test can be seen in Figure 1. The cone angle is defined as

$$\theta_{cone} = \arccos\left(\frac{|B_x|}{|B|}\right) \quad (4)$$

which, in the case of subsolar point, is identical to θ_{Bn} since the bow shock normal vector \hat{n} is pointing in the x direction.

As shown in Figure 1, there are distinct magnetosheath characteristics associated with the quasi-parallel and quasi-perpendicular bow shock. The high-energy ion flux is the one that is most noticeable, while the ion temperature anisotropy, and the magnetic field variance are also correlated with the change of the cone angle. The exact computation of these quantities can be found in Appendix A1. Interestingly, the region which is not shaded with any color is a typical example where the high-resolution measurements of MMS provide evidence of a short time scale change of IMF while the cone angle measurements of 1-min resolution fully miss the rapid change that is seen in the magnetosheath. The purpose of this example is to verify that the classification of jets into Qpar and Qperp can be performed using only local MMS measurements by comparing with a proxy for θ_{Bn} . MMS1 is located at $(11.37, -0.02, -1.01)R_E$ in GSE coordinates. This position was chosen to be close to the subsolar region. This was done to minimize the difference between θ_{cone} and θ_{Bn} while limiting the time shift effect from the bow shock to MMS position.

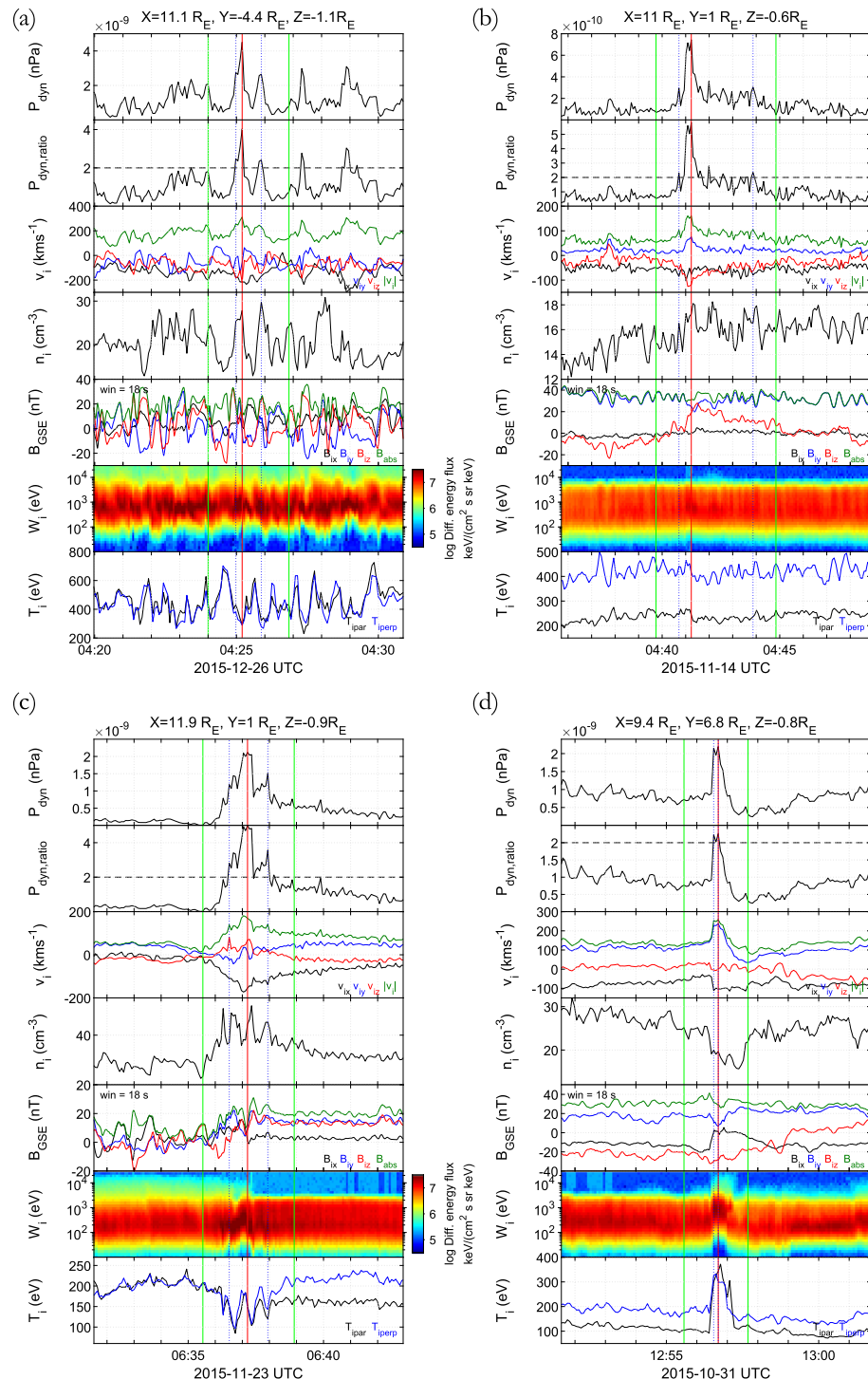


Figure 2. Examples of the four main categories of jets. (a) Quasi-parallel, (b) Quasi-perpendicular, (c) Boundary, and (d) Encapsulated jet. From top to bottom, in each subplot: dynamic pressure, ratio of the dynamic pressure to the background level, ion velocity, ion number density, magnetic field components averaged with a moving window of 18 s, ion energy spectrum, and parallel and perpendicular components of ion temperature. The red vertical line shows the time of maximum dynamic pressure, blue vertical lines the jet period, and green vertical lines indicate the prejet and postjet times. Finally, the black dotted line on the second panel of every subplot indicates a 200% enhancement of dynamic pressure compared to the background.

Typical examples of each jet class can be seen in Figure 2. In Figure 2a, we show a quasi-parallel jet, whereas in Figure 2b a quasi-perpendicular one. A boundary jet can be seen in Figure 2c and finally an encapsulated one in Figure 2d.

3.3.1. Prejet and Postjet Periods

The classification scheme is based on the assumption that there are three distinct phases in the jet phenomenon. Since the jet crosses MMS, observations include the plasma environment propagating in front of the jet, the jet flow, and the plasma behind the jet. These plasma environments are called, prejet, jet and postjet periods, respectively.

The jet period is the duration in which the criterion of Equation 1 is satisfied. In the case that the jet contains only one data point (~30%), we readjust the starting and ending point of the jet to include one extra data point before and after the jet, respectively. The prejet period is a period of time before the actual jet which is usually characterized by a gradual increase in dynamic pressure. The postjet period is an equally long period of time, characterized by a gradual drop of dynamic pressure associated with a nonjet magnetosheath region.

The prejet/postjet time periods are set based on jet duration as

$$\Delta t_{\text{pre,post}} = \begin{cases} 45\text{s}, & \Delta t_{\text{jet}} < 45\text{s} \\ 60\text{s}, & 45\text{ sec} \leq \Delta t_{\text{jet}} < 75\text{s} \\ 75\text{s}, & \Delta t_{\text{jet}} \geq 75\text{s}. \end{cases} \quad (5)$$

It was decided to have the prejet/postjet time increasing with jet duration mainly to assist the classification routine which is categorizing data points and chooses the class of each jet based on the percentage of them that fit the classification criteria. Furthermore, by manually inspecting cases of extensive duration jets ($\Delta t_{\text{jet}} > 45\text{ sec}$) we found that a slight increase to their pre/post jet times made the classification algorithm more accurate.

3.3.2. Verification and Validation of Data Set

In order to determine the settings for the classification scheme, a test data set was created through visual inspection, containing jets of every class. After testing the accuracy of our classification procedure the best stage from which the output was sufficient to derive statistical results was chosen (Appendix B1).

As a final validation, a visual inspection accompanied by a manual reclassification was made for a few misclassifications that the automatic procedure produced (~10–20%). This resulted in some slight changes to the data set while ensuring that the accuracy of the classification is satisfactory. Typically, the majority of automatic misclassifications were found in the boundary and encapsulated cases. This was expected since these classes had much more precise criteria to be met both in the jet and in the surrounding plasma region. More information regarding the verification of the data set and the accuracy determination of the procedure can be found in Appendix B1 and in the supporting information.

The number of jets in the final classified data set is shown in Table 3.

The position for all the main class jets is shown in Figure 3. There, the MMS position at the time of observation of the maximum dynamic pressure is shown. The magnetopause and bow shock regions are plotted based on the model found in Chao et al. (2002) and by using the average solar wind conditions that were found for all the jets in the data set. In particular, the model used here and below uses the following quantities. For the magnetopause model, the model uses the z component of the interplanetary magnetic field (B_z) and the ion dynamic pressure (P_{dyn}). In addition, the bow shock model also uses the magnetosonic Mach number (\mathcal{M}_{ms}) and the beta plasma parameter (β). For the average model shown in Figure 3, the conditions used are, $B_z = -0.075$ (nT), $P_{\text{dyn}} = 2.07$ (nPa), $\mathcal{M}_{ms} = 5.97$, and $\beta = 2.45$.

3.4. Derived Quantities

In order to derive statistical results for each of the classes, the “final cases” listed in Table 3 are used. These jets met all necessary criteria from the automatic procedure and have also been manually verified. As a result, unless explicitly mentioned, we use the verified (“final”) cases for our analysis. Finally, when we are referring to “main” classes we mean the four classes described in Table 2. More information regarding the criteria and the exact determination of these cases are given in the appendices (Appendices A1 and B1) of this article and in the supporting information.

Table 3
Classified Data Set of the Magnetosheath Jets for the Period September 2015 to April 2019

Subset	Number	Percentage (%)
Quasi-parallel	2,284	26.9
Final cases	860	10.1
Quasi-perpendicular	504	5.9
Final cases	211	2.5
Boundary	744	8.8
Final cases	154	1.8
Encapsulated	77	0.9
Final cases	57	0.7
Other	4,890	57.5
Unclassified/Uncertain	3,499	41.2
Border	1,346	15.8
Data Gap	45	0.5

Note. Using as initial data set the combined ($N = 8,499$) jets of Table 1. The properties of each class are shown in Table 2.

For all the jets, different variations of the minimum, mean, and maximum values of their properties are investigated. Most importantly, an analysis on how these quantities are distributed compared to the background magnetosheath plasma is being done. This analysis is conducted by introducing “difference” values, referring to quantities that are either maximum, mean, or minimum within a jet from which a 5-min background magnetosheath value is subtracted.

$$\Delta X_{(max/mean/min,5)} = X_{max/mean/min} - \langle X \rangle_{MSH}. \quad (6)$$

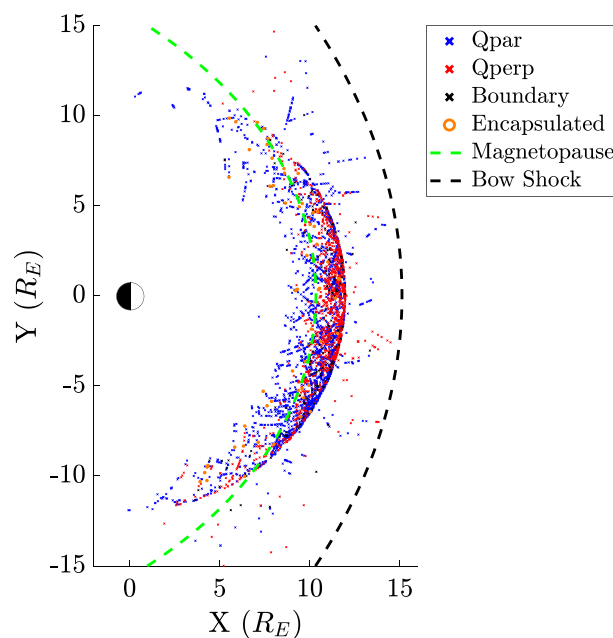


Figure 3. Location of the four magnetosheath jet classes projected to the xy -plane in GSE coordinates, identified in MMS data between May 2015 and May 2019. The green and black dashed lines mark the approximate location of the magnetopause and the bow shock during solar wind conditions averaged over the periods that a jet was found. Coordinate system is the Geocentric Solar Ecliptic (GSE) and both axes are normalized to Earth radius ($R_E = 6.371$ km).

In the background value ($\langle X \rangle_{MSH}$), we remove the jet period. As a result,

$$\langle X \rangle_{MSH} = \frac{1}{2n} \sum_i^n (X_{t_{start}-i} + X_{t_{end}+i}) \quad (7)$$

where start/end is the starting and ending point of the jet period, and $n = 33$ measurements.

The differences between the mean and max values were, statistically speaking, insignificant due to the short duration of the jets. Therefore, in order to make the visualization easier, the maximum values are primarily shown. It should be noted that the “difference” values (Equation 6) can give insight in the cases of Qpar and Qperp jets but should be treated with caution when referring to the boundary and encapsulated jets. The reason is that the background normalization in the first two cases is being done with plasma which is more or less similar throughout the 5-min period that was taken. On the other hand, for the boundary and encapsulated cases, due to the nature of plasma being different between the jet and the surrounding measurements, the difference values can be unreliable.

To determine the distance of each jet from the bow shock, a model for every jet based on its associated solar wind values was generated. The average associated solar wind conditions are derived from values 10 min before the jet and up to 5 min after. The asymmetric usage of measurements before and after the jet was done to compensate for the time plasma takes to travel from the bow shock to the MMS position. Later, the maximum velocity vector (\mathbf{V}_{max}) of each jet was used to propagate it back in time until a bow shock crossing was found. This procedure took ΔT_{BS_i} time for each jet (i) which was calculated as the number of steps multiplied by the time resolution of the FPI instrument (4.5 s). After approximating a point of origin for each jet, the distance from the bow shock is computed as

$$\Delta X_{BS} = X_{BS} - X_{MMS} \quad (8)$$

where X can be radial distance (R), distance along the yz plane (ρ), or distance along the x axis (X). It should be noted, that the modeled position of the bow shock may have a significant error as shown in several studies (e.g., Merka et al., 2003; Turc et al., 2013) and therefore any statistical results should be considered with caution.

Furthermore, the algorithm which computed the point of origin for each jet, assumes that no breaking nor change in the direction of the jet occurred from its creation until its observation by MMS. This assumption is certainly not ideal and it produced some cases where the jet was found to originate from a nonphysical origin (e.g., $\Delta R > 30 R_E$). In these cases, we used the dominant component of the velocity to propagate the jet to the bow shock as an alternative option. However, there were cases that still provided unphysical results. An algorithm identified these cases by checking whether the origin was extremely far away from the position the jet was found or if the time it took a jet to reach the bow shock was more than 30 min. In these cases, we simply removed the jet from this specific analysis. This procedure reduced the number of jets in all classes slightly. Specifically, four Qpar, two Qperp, two boundary, and one encapsulated jets were removed.

Similarly, a magnetopause model was generated using the model by Chao et al. (2002) and the solar wind conditions at the time of each jet observation. The magnetopause model, while also prone to several errors, can provide vital information regarding the relative position of jets of different classes. After, modeling the magnetopause for each jet, the radial distance from the closest point was measured as

$$\Delta R_{MP} = R_{MP} - R_{MMS} \quad (9)$$

where, R_{MP} is the closest point of the magnetopause to the position of MMS $R_{MMS} = (X, Y, Z)$.

Throughout the text, when referring to subsolar jets an extra criterion is applied:

$$\begin{aligned} |Y_{GSE}| &< 2R_E \\ |Z_{GSE}| &< 2R_E \end{aligned} \quad (10)$$

where $|Y_{GSE}|$ and $|Z_{GSE}|$ are the absolute values of the y and z coordinates of the MMS satellite at the time of maximum dynamic pressure of each jet. Applying this criterion generated a smaller subset of jets ($n = 298$). This set is used to investigate relations between distances from the bow shock. We do so because

a jet close to a subsolar position with a dominant x velocity component is more likely to have traveled a distance approximately equal to the x distance between MMS and the bow shock.

To investigate the orientation of the flow, we calculate two more quantities. First, we calculate the velocity in the yz plane (V_ρ), and then the angle between that velocity and the x axis. The velocity V_ρ is defined as

$$V_\rho = \sqrt{V_y^2 + V_z^2} \quad (11)$$

while the angle is defined as

$$\theta_{V_\rho} = \arctan\left(\frac{V_\rho}{|V_x|}\right). \quad (12)$$

An interesting quantity we investigated is the angle between the magnetic field vector before and after the jet. This was done in order to search for any interesting properties that could link a jet class to the pressure pulses connected to rotational discontinuities that were first described by Archer et al. (2012). To calculate the magnetic field angle we took the average of the magnetic field vector for 30 s, 1 min, and 2 min before and after the jet and determined the angle between the “averaged” magnetic field measurements. All the derived quantities provided similar average and median results, although the actual values varied slightly. We have decided to use the 30 s averaged magnetic field for the computation of the presented magnetic field angle.

$$\theta_B = \arccos\left(\frac{\langle \mathbf{B} \rangle_{\Delta t_1} \cdot \langle \mathbf{B} \rangle_{\Delta t_2}}{|\langle \mathbf{B} \rangle_{\Delta t_1}| |\langle \mathbf{B} \rangle_{\Delta t_2}|}\right) \quad (13)$$

where Δt_1 is a 30-s duration before the jet and Δt_2 a 30-s duration after the jet.

Another quantity that is considered is the angle between the average velocity vector of the jet and the velocity vector of the surrounding plasma. This is computed by taking the average vector of the jet period and finding its angle to the average velocity vector taken 5 min before and after the jet. In order to have a velocity that better characterized the background flow of the plasma, we removed 30 s before and after the jet when computing the average background velocity vector.

$$\theta_V = \arccos\left(\frac{\langle \mathbf{V} \rangle_{\Delta t_{jet}} \cdot \langle \mathbf{V} \rangle_{\Delta t_2}}{|\langle \mathbf{V} \rangle_{\Delta t_{jet}}| |\langle \mathbf{V} \rangle_{\Delta t_2}|}\right) \quad (14)$$

where, Δt_{jet} is the jet period and Δt_2 is a 9-min duration, of 4.5 min before $t_{1,start} - 30$ s and after $t_{1,end} + 30$ s.

To investigate the total effect of each jet we calculated the integrated dynamic pressure over the jet's duration along the flow (total fluence) as

$$f_{total} = \int P_{dyn} \cdot |\mathbf{V}| \cdot dt = \sum_i^n P_{dyn,i} \cdot |\mathbf{V}_i| \cdot \Delta t \quad (15)$$

where, n is the number of measurements within each jet period and Δt is the time resolution of the FPI instrument (4.5 s).

We also present correlation coefficients between a number of jet properties. The most commonly used correlation coefficients are the Pearson's correlation coefficient (PCC) and Spearman's rank correlation coefficient (ρ_{Sp}). The former describes a possible linear relationship between the two variables, while the second shows the strength of a monotonic relation (Myers et al., 2013). For our analysis, we use the Spearman's coefficient to determine correlations between jets' quantities.

Throughout the results section, all plots are color coded the same way. Qpar jets are represented by blue, Qperp by red, boundary by black, and encapsulated by orange.

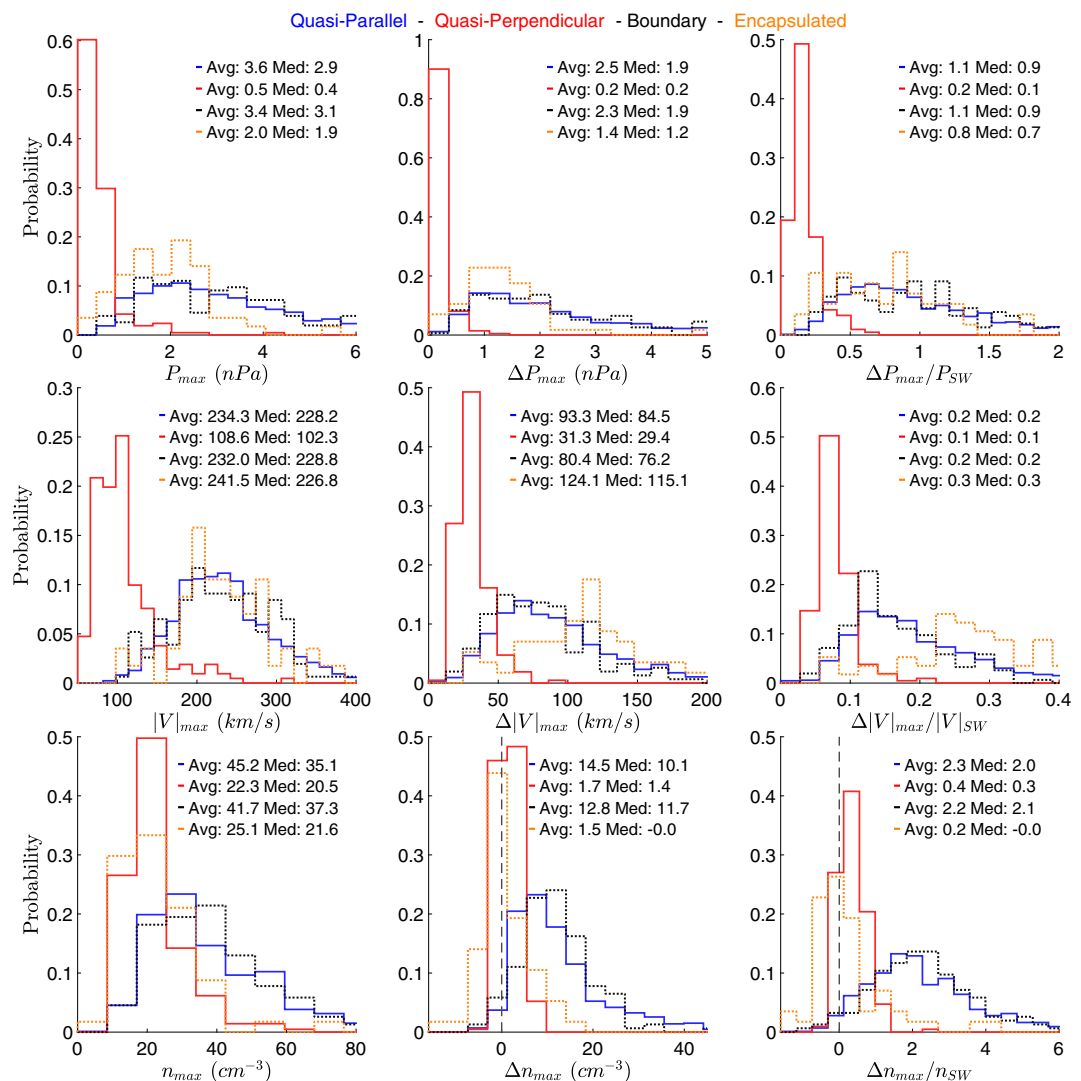


Figure 4. Histograms showing distributions, average, and median values for the maximum values of the basic jet quantities. Maximum dynamic pressure, absolute velocity, and density are shown. First column shows the measured values, the second describes the difference from the background, and the third is normalized to the associated solar wind values.

4. Results

The first observation, as shown in Table 3, is that the number of jets found downstream of the quasi-parallel shock is significantly higher than the number found in other classes. Boundary and quasi-perpendicular jets are less frequent, and finally, encapsulated jets occur very rarely. While we cannot derive how frequently each jet occurs for each magnetosheath region (Qpar and Qperp), one can assume that on average the magnetosheath region during MMS orbits is equally distributed between the two regions (Petrinec, 2013). With that assumption, we can estimate that quasi-parallel jets occur much more frequently than quasi-perpendicular jets. Specifically, they can occur \sim 5–10 more often, depending on how many of the uncertain jets could be classified as Qpar jets (41.2% of the detected jets are unclassified, see Table 3). This result is in agreement with recent results showing that the frequency of Qpar jets can be \sim 9 higher than Qperp jets (Vuorinen et al., 2019).

4.1. Properties of the Jet Classes

In Figures 4–10, the basic properties of each class along with the quantities defined in the previous section are shown.

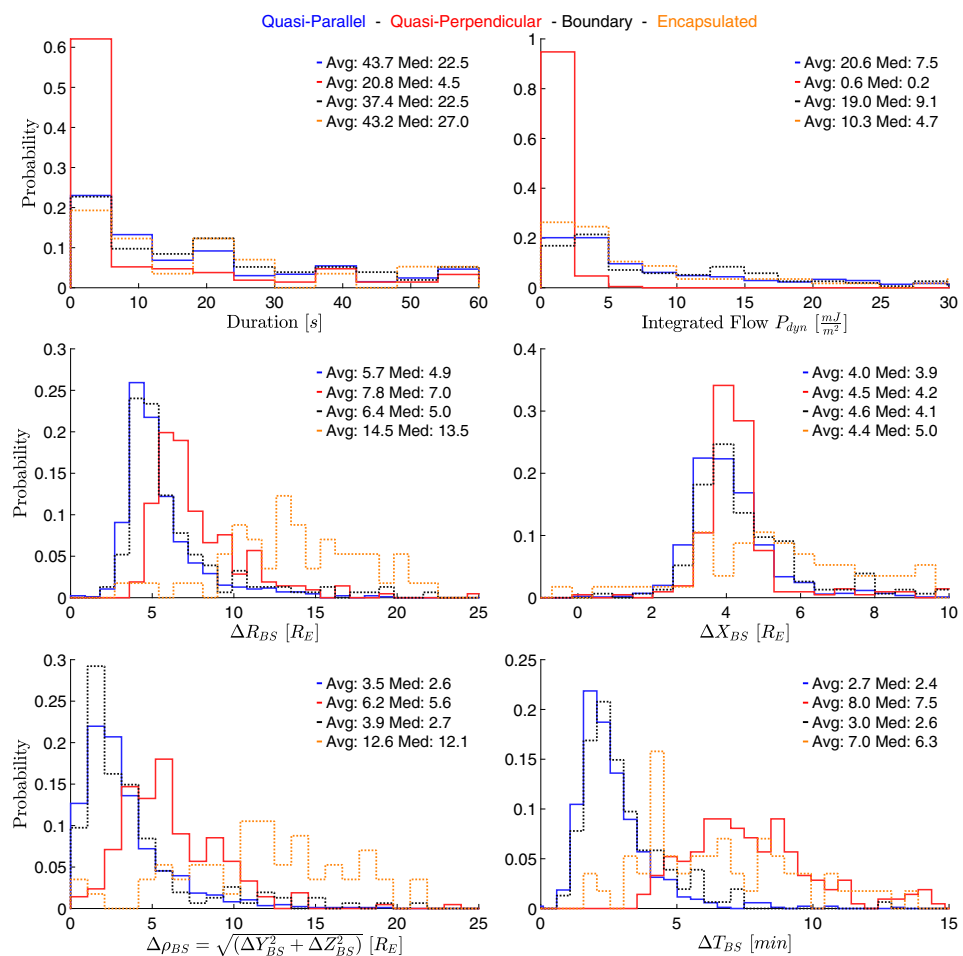


Figure 5. Histograms showing distributions, average, and median values for scale sizes and for distances, estimated from a point of origin at the bow shock for each jet. ΔT_{BS} describes the time that was estimated for the jet to arrive to MMS from its origin point at the bow shock.

Starting with the basic properties of the jets in Figure 4, quasi-parallel and boundary jets have on average much higher dynamic pressure ($\langle P_{max} \rangle \sim 3$ nPa) compared to the quasi-perpendicular jets (~ 0.5 nPa), while encapsulated jets lie somewhere in between. Similar contrast between classes can be observed for the differences in dynamic pressure from the background magnetosheath plasma with or without solar wind normalization. The distributions and the average values of the absolute ion velocity show that the velocities of Qperp jets are much lower than these of Qpar, boundary, and encapsulated jets. Interestingly, while this effect holds regardless of the normalization technique, when normalizing to the solar wind, the difference in velocity between classes is reduced. This could mean that on average the velocity of a jet primarily depends on the solar wind velocity at the time of its formation. Furthermore, it shows that the majority of Qperp jets are found under low solar wind velocities. Regarding the ion density, Qpar and boundary jets have on average twice as high density as the Qperp and encapsulated jets. When looking at the difference values, however, the actual density gain is an order of magnitude more for the Qpar and boundary cases compared to the other two. Finally, the overall net gain of density and velocity for the jets is much higher for the rest of the classes compared to the Qperp jets.

In general, Figure 4 shows that the properties of Qpar and boundary jets are very similar, while both velocity and density changes in the Qperp jets are much smaller. This could imply differences in their generation mechanisms. Finally, encapsulated jets are dominated by an increase in velocity with absolute velocities gain being even higher than Qpar jets while their density distribution is very similar to Qperp jets.

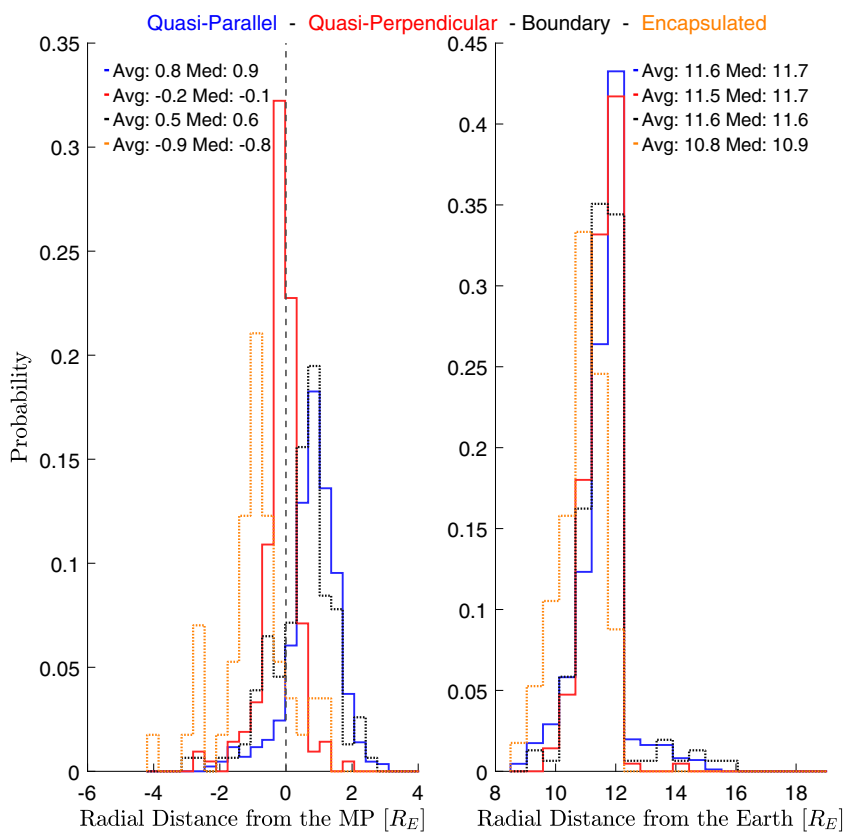


Figure 6. Histograms showing distributions, average, and median values of the jets' distance (left) from the magnetopause and (right) from the Earth.

For all jet classes, there are several jets where the dynamic pressure reaches values even higher than the dynamic pressure of the solar wind as expected from earlier studies (Plaschke et al., 2013). Only one encapsulated jet was found to have a higher velocity than its associated average solar wind velocity, while all other jets had a lower one. We can conclude that the main contribution of the dynamic pressure increase compared to the solar wind is due to the compression that solar wind undergoes after interacting with the bow shock. This, in turn, causes a density increase that can be several times higher in the jets compared to the solar wind.

The average and median jet duration of the main class jets is found to be 39 and 18 s, respectively. As shown in Figure 5, Qpar and encapsulated jets have a slightly longer duration than boundary jets, while the Qperp jets have a much shorter duration, with the majority consisting of only one data point which corresponds to 4.5 s. To investigate the low duration of Qperp jets, we explored the statistical properties of Qperp jets that contained at least three data points (69/211 cases). Doing so, we discovered that their basic properties (Figure 4.) are statistically similar to the whole subset and therefore it was decided that all the jets can be included in the analysis. It should be noted that the duration of encapsulated jets is biased to appear longer by their definition (Table 2), since shorter jets would be classified as Qpar.

In Figure 5, when looking at the dynamic pressure integrated over the jet period (Equation 15) we see a consistent picture where the shorter duration along with the lower dynamic pressure make the Qperp jets much weaker in comparison to the rest of the jet classes. On average the rest of the jets seem to be similar while the Qpar and boundary jets, again hold very similar properties. The distance from the bow shock (Equation 8) is quite different for each class. While boundary and Qpar have similar relative positions, the Qperp jets are found further inside the magnetosheath. This difference is more visible when looking at the distance on the yz plane from the bow shock. Encapsulated jets are also found at a much higher radial distance (R) from the bow shock, again with the ρ component having much higher values than the rest of the classes. It should be noted that Qperp jets are found to occur primarily under low-velocity solar wind conditions. As a result, the bow shock model used for those cases generates a bow shock further away from

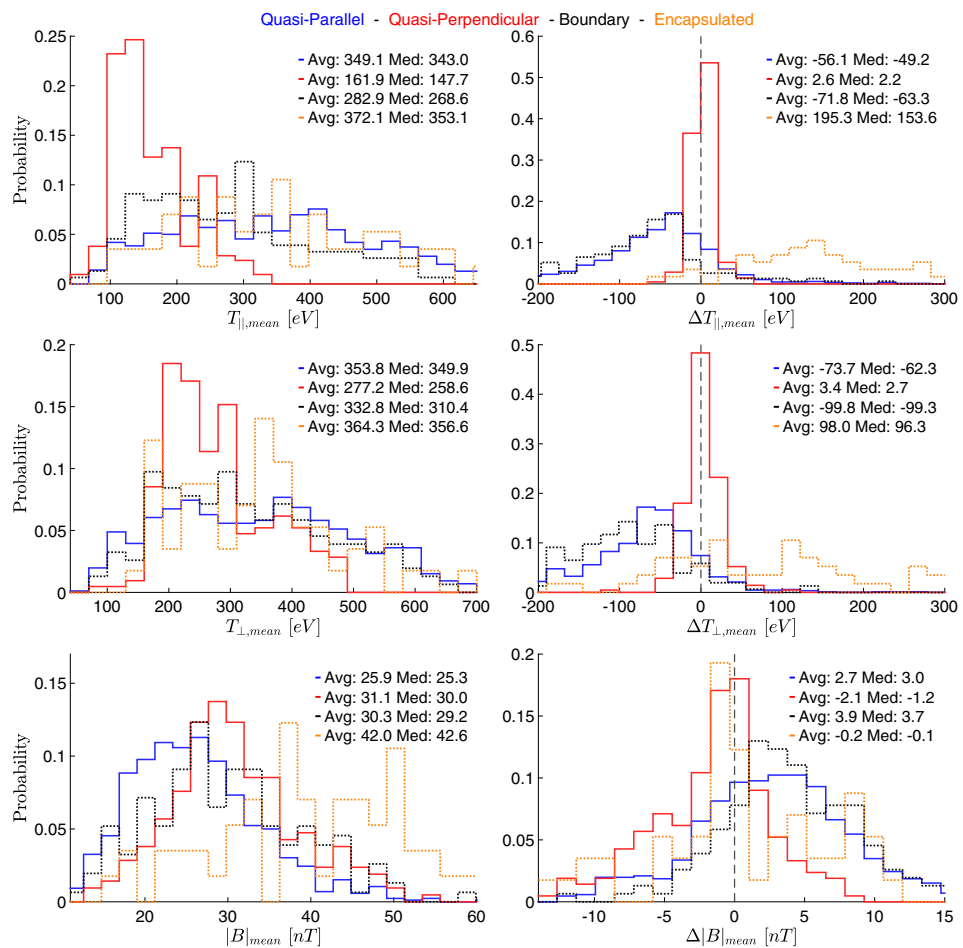


Figure 7. Histograms showing distributions, average, and median values for the average values of (top and middle rows) ion temperature and (bottom row) absolute magnetic field.

the Earth than for the cases of Qpar and Boundary jets. Finally, the time that it took each jet to reach the MMS is much different. Qpar and boundary jets need on average ~ 3 min while the much slower Qperp jets require much more at around ~ 8 min. Encapsulated jets also take a long time to reach MMS from their origin point (~ 7 min) but in contrast to Qperp jets, this is due to the large distance that they have to cover rather than their velocity.

To analyze the different geometric properties of each class, we also include Figure 6, showing the distance of the jet from the Earth and the distance from a magnetopause model (Equation 9). It is shown that while jets of every class are found in similar distances from the Earth (position of MMS), the distance from the magnetopause varies considerably. While Qperp jets are expected to appear closer to the magnetopause from their corresponding distance of the bow shock (Figure 5), it is now clear that they occur so close to the magnetopause that often they appear to be within the magnetosphere due to the inaccuracies of the model in use. It should be stressed that encapsulated jets are not only found close to the magnetopause but also found closer to the Earth (Figure 6, right).

Figure 7 shows that the ion temperature profiles are quite different between each class. On average, the temperature is lower on Qperp jets (~ 100 eV) compared to the rest of the jets (~ 300 eV). The difference of both T_{\perp} and $T_{||}$ compared to the background is negative and very similar between boundary and Qpar jets. On the other hand, it is around zero for Qperp jets and positive for the encapsulated jets. Most of the observed differences are expected due to the nature of the magnetosheath region and from the definition of each class. As mentioned in the previous subsection, encapsulated and boundary jets have a very different background magnetosheath. Therefore, a direct comparison between each class can be misleading, especially in the case of the highly variant temperature measurements.

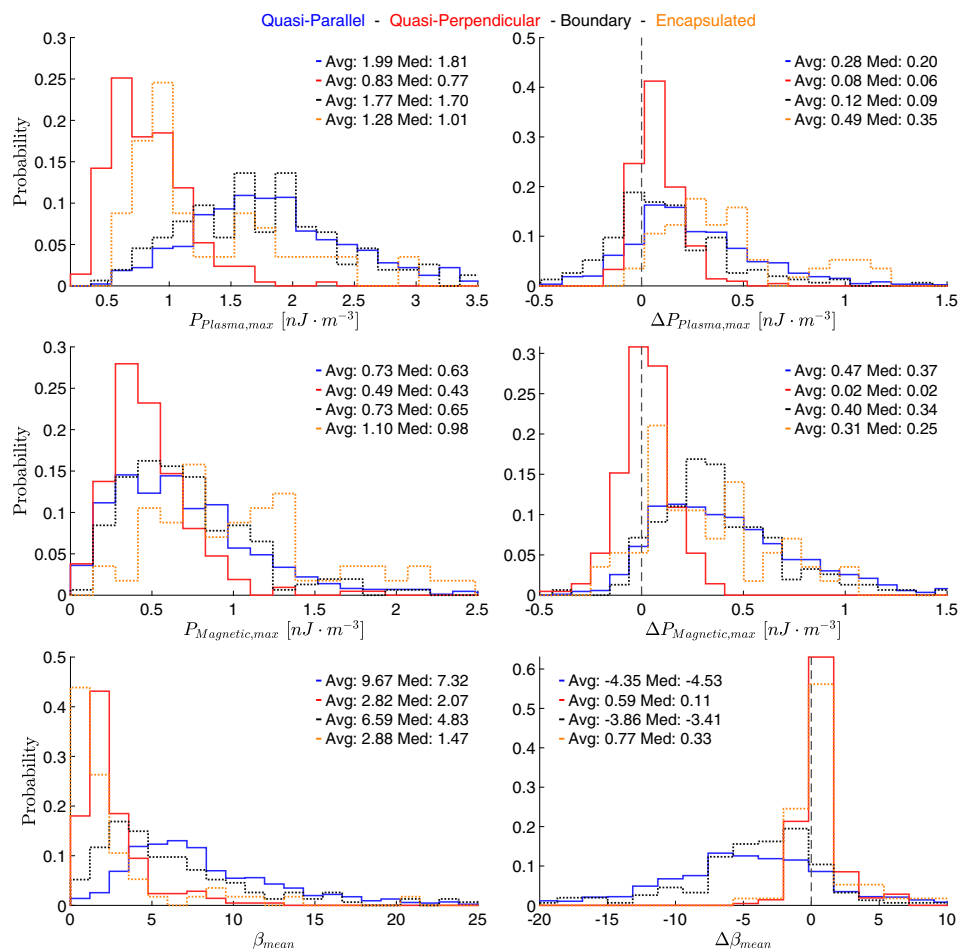


Figure 8. Histograms showing distributions, average, and median values for the (top row) maximum plasma pressure, (middle row) the maximum magnetic pressure, and (bottom row) the mean β parameter.

An interesting difference regarding the mean absolute magnetic field appears in Figure 7. Qpar jets have on average, a smaller mean absolute magnetic field than the rest of the classes ($\langle |B|_{mean} \rangle \sim 25$ nT). Encapsulated jets have almost twice as high values, while the mean absolute magnetic field of Qperp and boundary jets' is in between, at $\langle |B|_{mean} \rangle \sim 30$ nT.

The difference in the mean absolute magnetic field ($\Delta |B|_{mean}$) is higher in Qpar and boundary jets compared to Qperp and encapsulated jets. Specifically, Qpar and boundary jets have a bigger absolute magnetic field than their background magnetosheath. On the other hand, Qperp jets have on average a slightly smaller magnetic field although the actual values range for individual events vary significantly ($\Delta |B|_{mean} \in [-10, 10]$ nT).

Figure 8 shows how plasma (thermal) and magnetic pressures vary between each class along with their ratio (β parameter). For all the classes, the maximum plasma pressure is on average higher than the maximum magnetic pressure. However, when looking at the difference values, the Qpar, and the boundary jets have higher maximum magnetic pressure ($\Delta P_{magnetic,max}$) than maximum plasma pressure ($\Delta P_{plasma,max}$). On the other hand, Qperp and encapsulated jets still have a higher maximum thermal pressure than maximum magnetic pressure difference. Looking at the maximum magnetic pressure and its difference to the background can also be directly interpreted as a measurement of the maximum absolute magnetic field. This information shows us that although from the previous histograms (Figure 7), the average magnetic field ($|B|_{mean}$) is higher in the case of Qperp jets, the maximum ($|B|_{max}$) values are higher in the Qpar and boundary cases. This could originate from the higher duration of Qpar jets, along with the higher time resolution of the FGM data compared to the FPI. These two factors can allow very high magnetic field values to occur within a jet period since in principle $|B|$ can have a higher variance in the quasi-parallel environment. The behavior of the β parameter is consistent with the previous results. While it is higher for

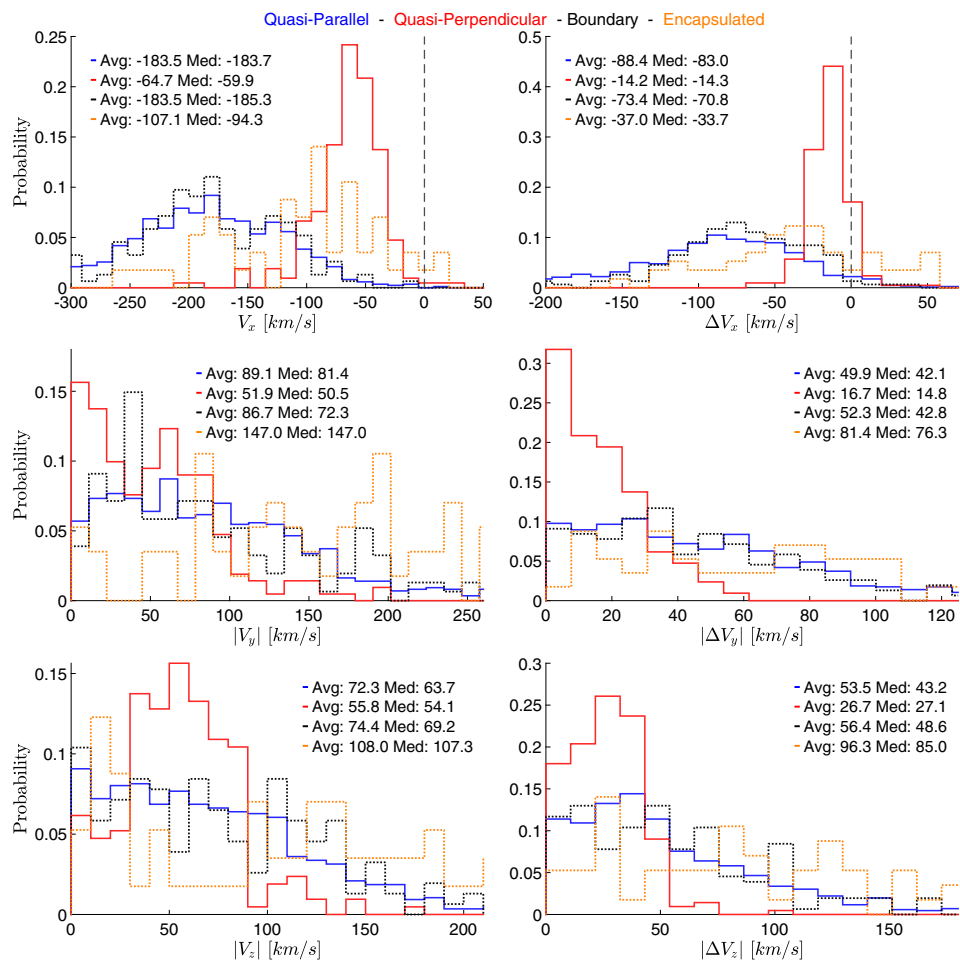


Figure 9. Histograms showing distributions, average, and median values for (top to bottom rows) each velocity component at $|V|_{max}$.

the Qpar and boundary classes, it is on average smaller than that of the background plasma around the jets. On the other hand, encapsulated and Qperp jets have on average smaller beta values but still maintain a positive difference when compared to the background.

Specifically, average beta values appear to be closer to unity for the Qperp and encapsulated cases, while they are on average higher ($\langle \beta_{qpar} \rangle \sim 10$, $\langle \beta_{boundary} \rangle \sim 6$) for the other classes. When looking at the difference to the background, it appears that Qpar and boundary jets have a negative beta difference ($\Delta\beta < 0$). This could indicate that magnetic pressure has a larger effect in the jet than in the surrounding magnetosheath plasma.

The velocity components of each class are shown in Figure 9. Here, we present the absolute velocity for the y and z component. This was done because all jets and especially encapsulated jets had a distribution that produced an average velocity close to zero, in both components, due to equally frequent jets exhibiting a high negative and positive $V_{y,z}$. As a result, providing a histogram without the absolute values would limit the information of each class and would not contribute to a meaningful comparison.

As expected, almost every jet has a dominating negative (earthward) x component, with the Qperp jets on average having smaller values on every velocity component compared to the other classes. Furthermore, Qperp jets seem to have very similar velocities in all three components which are different from the rest of the classes that tend to have a more significant imbalance between components. An interesting difference can be seen in the encapsulated jets where the dominant component of their velocity is surprisingly V_y and V_z . The same effect can be seen when we look at the absolute difference ($|V_{jet} - V_{MSH}|$), where the difference to the background seems to be higher for the Qpar and boundary jets than Qperp jets, while encapsulated exhibit values much higher than the rest of the classes.

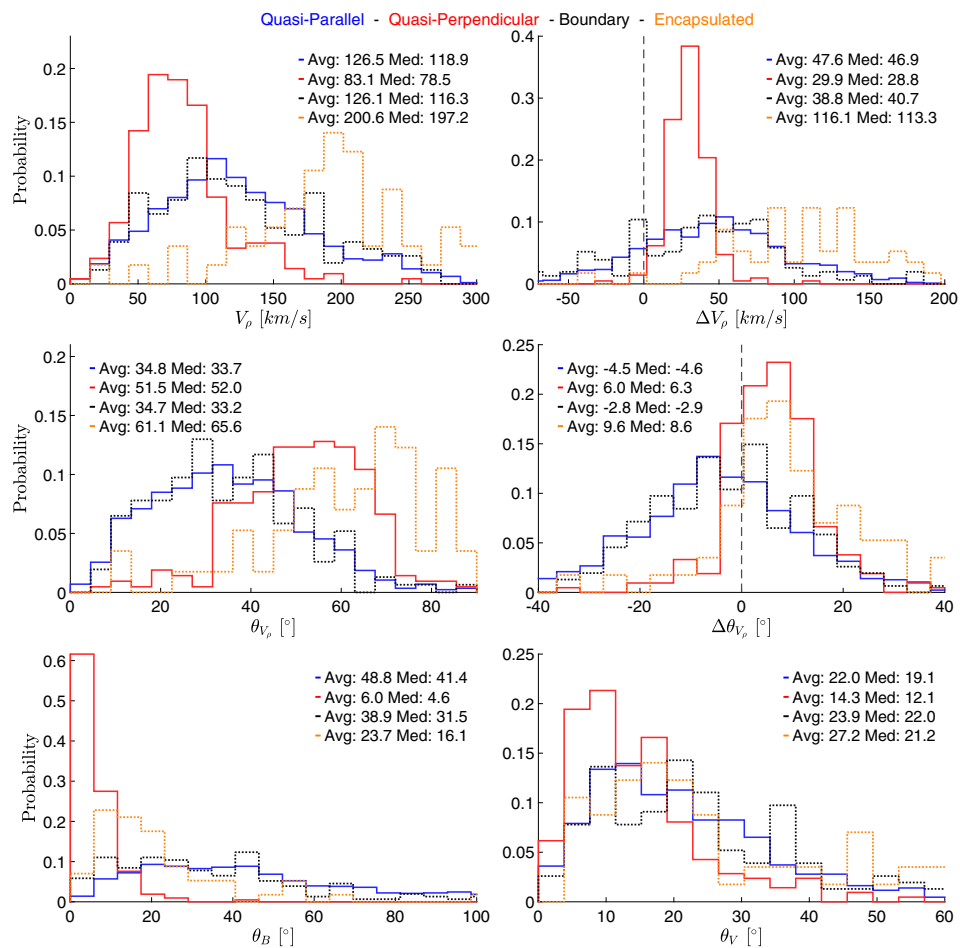


Figure 10. Histograms showing average and median values for directional information and changes in the (top row) magnetic field and (middle and bottom rows) velocity vectors. In particular, the angle between the x velocity component and the yz plane is investigated ($\theta_{V_{\parallel}}$). Furthermore, two angles showing the difference in the magnetic field vector (θ_B) and the velocity vector (θ_V) between the periods before and after the jet periods are also shown.

Finally, in Figure 10, directional information and rotation angles of the magnetic field and the velocity are given. As expected, the yz plane velocity (V_{\parallel}) is much higher for the encapsulated jets compared to the other three classes. This can also be seen when calculating the angle between the jet's velocity and the x axis (Equation 12), in which the Qpar and boundary jets show similar behavior, while Qperp jets have on average a higher angle and encapsulated jets the highest. This picture is consistent when comparing to the background plasma in which Qpar and boundary jets show a net decrease in the angle while Qperp and encapsulated show a net increase. Looking at the magnetic field rotation angle (Equation 13), there seems to be a significant difference between the Qperp jets and the other classes. Qperp have on average a very small ($\sim 6^{\circ}$) difference while the rest of the classes have on average higher values, particularly the Qpar jets. Considering velocity rotation angles (Equation 14), Qperp jets exhibit the least changes, although all classes seem to have similar statistical values and distributions.

It should be noted that since both velocity and magnetic field rotation angles describe the changes between the plasma before and after jet, the results are heavily affected by the duration of the jet. Specifically, it is expected that jets with a shorter duration such as Qperp jets would statistically have a smaller angle change since measurements taken are spatially and temporally closer to each other.

4.2. Relation Between Jet Properties

In this subsection, we will report on some observations on correlations between different jet properties. It should be noted that all correlations mentioned were found to have a p value of less than 0.01, unless stated

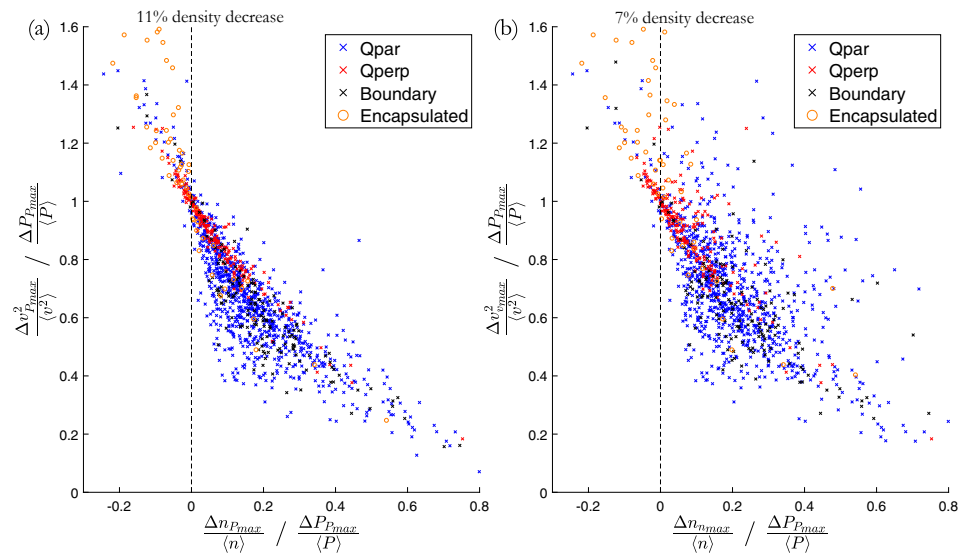


Figure 11. (a) Relative difference in density and velocity at the time of maximum P_{dyn} . (b) Relative difference in density and velocity for the maximum value of each quantity, measured within the jet period.

otherwise. The computation of the p value was done through the exact permutation distributions of each subset (Edgington, 2011).

There is a moderate correlation between the magnetic field rotation angle (θ_B) and both the maximum dynamic pressure (P_{max}) and the difference of maximum dynamic pressure compared to the background (ΔP_{max}).

Specifically, regardless of the way we calculated the magnetic field rotation angle, for all jets found in the main classes, we found a moderate correlation using Spearman's coefficient, $\rho_{Sp,All} = 0.43 \pm 0.02$. Considering only subsolar jets this correlation was increased, reaching $\rho_{Sp,Subsolar} = 0.6 \pm 0.05$.

A possible interpretation could be that the jets distort the magnetic field lines that are embedded in the plasma in front of them. On weaker jets such as in the majority of Qperp jets (Figures 4 and 10) this effect would be hardly visible since we see the dynamic pressure being an order of magnitude less compared to the other classes and the magnetic field rotation angle is also close to zero. On the other hand, on jets that on average have a higher velocity and density gain, magnetic field vector seems to be different in the plasma in front and behind the jet. To investigate this possible link, we look at class-specific correlation coefficients. For the classes of Qperp and Qpar jets, it was found that the correlation is almost nonexistent ($\rho_{Sp,\perp,||} = 0.1 \pm 0.05$ (p value = 0.04)). As a result, we conclude that the correlation was caused by the different properties of each class causing an artificial correlation that does not necessarily represent a physical property. The above result emphasizes the importance of classifying jets that physically occur in different environments before drawing any strong conclusions.

In Figure 11, a comparison between the density and the velocity squared difference normalized by the total dynamic pressure gain is shown, similar to Figure 3 of Archer and Horbury (2013). Figure 11a shows the relative change in density and velocity with measurements taken at the point of maximum dynamic pressure. In Figure 11b, however, the difference is taken by using the measurements of maximum density, velocity, and dynamic pressure for each quantity. As shown in Figure 11, the majority of the jets have a combination of velocity and density increase, contributing to the overall dynamic pressure enhancement. For the Qpar and boundary cases, less than 0.5% jets are purely velocity driven, exhibiting a density decrease compared to the background plasma. On the other hand, Qperp jets can have a decrease in density up to 22% and encapsulated jets up to 68% of the times, making their dynamic pressure to mainly originate from a velocity increase. More information regarding the velocity and density distribution of each class can be found in Table 4. As expected, most of the jets regardless of their class exhibit an increase in both density and velocity when comparing to the background magnetosheath. This result shows that the increased frequency of Qpar and boundary jets can be at least partially attributed to density enhancements taking place, while being

Table 4
Velocity and Density Distribution of Jets That Exhibit a Dynamic Pressure Increase

Class	Velocity decrease (%) $V_{V_{max}}(V_{P_{max}})$	Density decrease (%) $n_{n_{max}}(n_{P_{max}})$
All	1.6 (1.8)	6.9(10.9)
Main classes	0 (0)	7.3(10.8)
Quasi-parallel	0 (0)	2.9(5.23)
Quasi-perpendicular	0 (0)	15.6(22.3)
Boundary	0 (0)	3.9(5.2)
Encapsulated	0 (0)	50.1(68.4)

Note. First values are based on the maximum quantity met within jet's duration and values in parentheses are derived from the density and velocity value found at P_{max} .

insignificant or even absent in the case of Qperp jets. It should be noted that the values in parentheses shown in Table 4 correspond to the same time (P_{max}) and are therefore a better metric for quantifying the cases that exhibit a density decrease. However, the calculation that includes the maximum density and velocity points are also important as they are measured within the jet period as seen by MMS. These values act as the lowest limit case metric, showing how many jets exhibit an increase or decrease in velocity and density.

When comparing our results to earlier studies, we find that they are quite similar. In particular, depending on the normalization technique 7–11% of the jets exhibit a relative decrease in density with the increase in dynamic pressure being caused by a very high enhancement of absolute velocity. Plaschke et al. (2013) found 10.5% using a different jet criterion, while Archer et al. (2012) using essentially the same criterion as this work found 18%. In the main classes, we find no cases exhibiting a velocity decrease as shown in Figure 11 and Table 4. In order to see if there are any jets showing a velocity decrease, we searched the full jet database ($N = 8,499$). The only cases with a velocity decrease were 158 jets from which 151 have been classified as “Border” jets, found too close to either the magnetopause or the bow shock. Therefore, since any calculation averaging over different plasma regions is statistically unreliable, we exclude them. Careful examination on the rest of the seven cases showed that they were jets that occurred very close to another jet but not close enough to fulfill the criteria of jet combining (Equation 3). As a result, we conclude that there are no jets showing a relative velocity decrease at their maximum dynamic pressure measurement.

In Figure 12 we present two different types of cross-plots. In subplots (a) and (c), plots of the difference in maximum density (Δn_{max}) against difference in maximum magnetic field ($\Delta |B|_{max}$) with and without solar wind normalization are shown. This was done in order to test a hypothesis that connects SLAMS to the generation of Qpar jets (Archer et al., 2012; Karlsson et al., 2015). We, therefore, search for some kind of correlation between the density increase and the magnetic field increase since SLAMS have such a correlation (Behlke et al., 2003; Schwartz & Burgess, 1991). In the subfigures (b) and (d) we similarly investigate the difference of maximum velocity (ΔV_{max}) against the difference in minimum ion temperature (ΔT_{min}). This was done to see if a correlation can be found that could support the mechanism proposed by Hietala et al. (2009) that associates jets with ripples of the quasi-parallel bow shock. As discussed and shown in earlier studies, it is expected that the background plasma surrounding the ripple-generated jet would be more decelerated and would, in turn, have a higher temperature compared to the jet flow created by passing through a ripple of the bow shock, undergoing less deceleration, and heating (Hietala & Plaschke, 2013; Plaschke et al., 2013).

As shown in Figures 12a and 12c, for the quasi-perpendicular jets, there is no significant correlation between the difference in maximum magnetic field (ΔB_{max}) and the difference in maximum density (Δn_{max}). However, in the case of quasi-parallel jets, there is a moderate monotonic relationship between the two quantities. Spearman's rho value (ρ_{Sp}) for the quasi parallel case is $\rho_{Sp,a,||} = 0.57$ and $\rho_{Sp,c,||} = 0.55$, whereas for the quasi-perpendicular jets is $\rho_{Sp,a,\perp} = -0.2$ and $\rho_{Sp,c,\perp} = -0.27$. For all the jets together, a total correlation of $\rho_{Sp,a} = 0.66$ and $\rho_{Sp,c} = 0.63$ is reached. Indices *a*, *b*, *c*, *d* refer to the subplots of Figure 12, while the symbols of parallel and perpendicular refer to Qpar and Qperp jets, respectively.

These results support the idea that a subset of quasi-parallel jets may originate from a SLAMS interacting with bow-shock ripples as described by Karlsson et al. (2015). Further support of this mechanism is shown when looking back at the general characteristics of each class. In Figure 4 it is shown that Δn_{max} is an order

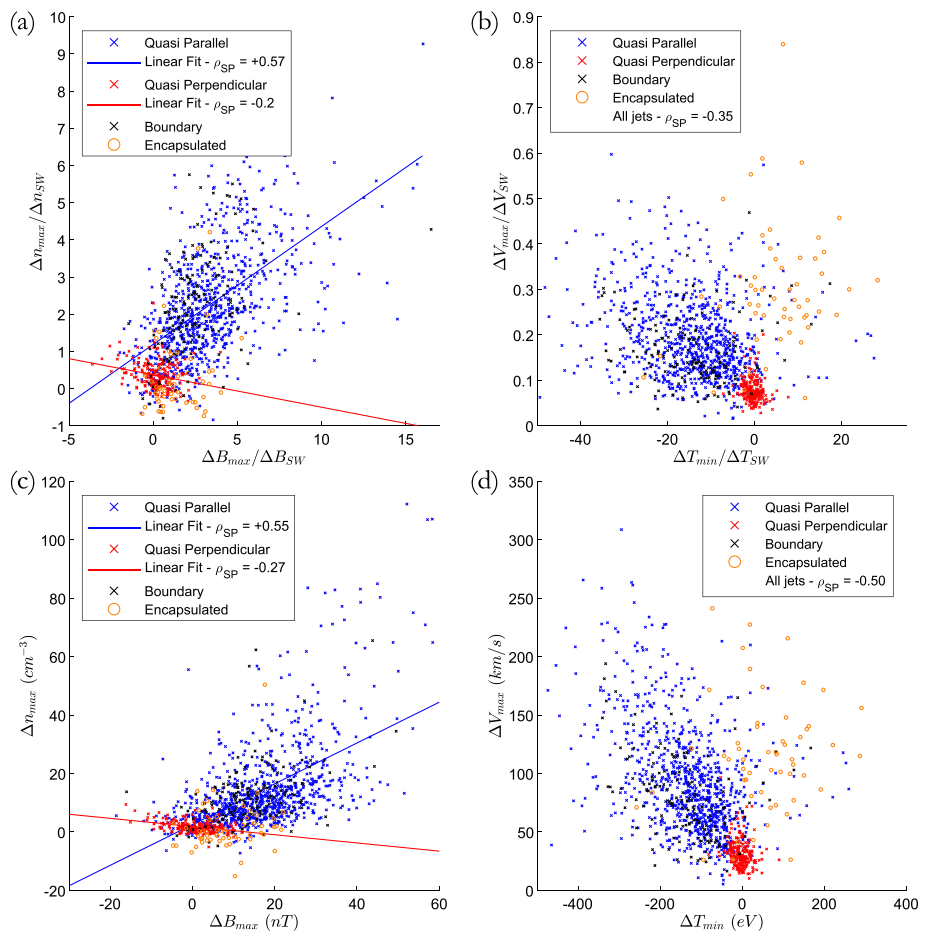


Figure 12. (a) Δn_{max} against $\Delta|B|_{max}$ normalized over solar wind data. Linear regression lines are shown for visual guidance, for the Qpar (blue) and Qperp (red) cases. (b) ΔV_{max} against ΔT_{min} normalized over solar wind data. (c) Δn_{max} against $\Delta|B|_{max}$. Linear regression lines are shown for visual guidance, for the Qpar (blue) and Qperp (red) cases. (d) ΔV_{max} against ΔT_{min} . In all figures every point represents a jet while the color shows its class.

of magnitude higher for the Qpar jets compared to the Qperp. Furthermore, in Figure 7, Qpar jets exhibit on average a positive difference on the average absolute magnetic field compared to the Qperp jets that do not. Maximum magnetic pressure and average β values shown in Figure 8 also support SLAMS since Qpar and boundary jets have not only a higher magnetic pressure than Qperp jets, but also a higher value than their surrounding plasma. It should be noted, however, that the anticorrelation observed for Qperp jets cannot be directly explained through any known mechanism. The observed anticorrelation should be treated with caution since it was only found for the “final cases” of Qperp jets (Table 3). When we look at the whole body of Qperp jets the observed correlation disappears.

In Figures 12b and 12d a weak/moderate linear correlation between the difference in minimum temperature (ΔT_{min}) and the difference in maximum absolute ion velocity (ΔV_{max}) is shown. Correlation coefficients are found to be $\rho_{Sp,b} = -0.35$ and $\rho_{Sp,d} = -0.5$ when looking at the whole body of the jets. While looking exclusively at Qpar jets, we find $\rho_{Sp,b,\parallel} = -0.28$ and $\rho_{Sp,d,\parallel} = -0.43$. On the other hand, when looking at Qperp jets, we find correlation coefficients of $\rho_{Sp,b,\perp} = -0.24$ and $\rho_{Sp,d,\perp} = -0.23$.

All main class jets have a small to medium anticorrelation relation between the ion temperature and the velocity difference within the jet period (Figures 12b and 12d). As discussed previously, we can interpret this result as indirect support of a mechanism that is based on the bow shock ripple idea (Hietala & Plaschke, 2013; Hietala et al., 2009). This result is also supported by the general properties shown in Figure 7, where for Qpar jets there is a larger difference between the temperature of the background magnetosheath plasma and the jet. Finally, it has been recently found that similar ripples can be found also at the quasi-perpendicular

bow shock which could mean that the generation mechanism of these jets is of the same nature (Johlander et al., 2016). Although the majority of the jets seem to have a medium anticorrelation that could support Hietala's mechanism (Hietala & Plaschke, 2013; Hietala et al., 2009), we cannot say the same for the quasi-perpendicular where the anticorrelation is weaker. It should be noted, however, that due to the very small duration of the jets, there is usually only one measurement for the temperature and the velocity. Therefore, there is a higher uncertainty regarding this result compared to the other classes.

Finally, based on the differences between thermal and magnetic pressure shown in Figure 8, we investigate possible relationships with other jet properties.

Regarding the difference in maximum magnetic pressure, there is a moderate to strong correlation with the total integrated dynamic pressure $\rho_{Sp,All} = 0.72$. This result could be interpreted in terms of SLAMS similarly to the analysis of Figure 12 since to calculate the total dynamic pressure we include the ion density (n). However, it was found that all the factors of Equation 15 are correlated to the maximum magnetic pressure ($P_{mag,max}$), including the difference in maximum absolute velocity (ΔV_{max}) which had a correlation coefficient of $\rho_{Sp,All} = 0.59$ and the duration which had a correlation of $\rho_{Sp,All} = 0.62$. This result is unexpected and can be considered an indication that magnetic forces play a more important role than previously thought. Qpar jets have similar correlations, while Qperp jets are also alike, apart from the same anticorrelation shown in Figure 12, regarding the density difference and $\Delta|B|$. It should be noted that this effect appears on all the jets and not only in the Boundary jets as initially speculated.

However, when looking at each class exclusively, the results show that the effect decreases significantly for the duration and velocity for both Qpar and Qperp jets $\rho_{Sp} \sim 0.2$. The correlation (when taking all classes together) seems to have been artificially created because in jets with higher velocities and duration it is relatively easier to measure the magnetic field in higher values. This is made possible by the fact that longer duration jets could in principle allow more measurements of the magnetic field to occur and due to the variance of the FGM measurements, reach a higher peak. This, in turn, creates a nonphysical correlation between the maximum magnetic field measurement found within a jet and its duration. The only effect that seems to be robust and even enhanced when taking average quantities is the correlation between the density difference ($\Delta n_{mean,max}$) and the absolute magnetic field difference ($\Delta|B|_{mean,max}$). Specifically, Qpar jets have a positive correlation in all four possible combinations of the absolute magnetic field and ion density quantities. The four combinations result when taking the average and maximum density and test their correlation with the average and maximum absolute magnetic field. Looking at these pairs, it is found that Qpar maintain a positive correlation coefficient, $\rho_{Sp,||} \in [0.3, 0.6]$. Similarly, the anticorrelation of the Qperp jets remains in all cases, $\rho_{Sp,\perp} \in [-0.28, -0.65]$. Once more, we should point out that the correlation found in the Qpar jets remains high even when looking at all the Qpar jets rather than the "final cases" (Table 3). On the other hand, the observed anticorrelation is considerably smaller for the Qperp jets.

From this result, we conclude that the magnetic field seems to play an important role in forming the density profile of each class, possibly explained through SLAMS mechanism. The correlation found on other jets' properties although less consistent, could still indicate that magnetic fields could have a more important role regarding the velocity and duration of each jet.

An interesting difference was also found when investigating the difference in both the maximum and the average thermal plasma pressure difference ($\Delta P_{th,mean,max}$).

Qpar jets when investigated with the maximum differences in density and thermal pressure have a moderate correlation $\rho_{Sp,||} = 0.36$. However, when we take average values for density or thermal pressure, this correlation disappears fully. On the other hand, as discussed previously, density changes are heavily correlated with the magnetic pressure of the Qpar jets. This result shows that the changes in temperature are more important than the changes in density in deriving the thermal pressure difference. On the other hand, Qperp jets have a high correlation of density change and thermal pressure $\rho_{Sp,\perp} = [0.5, 0.7]$. This indicates that the contribution of density change in thermal pressure difference is more important than the temperature difference for the Qperp jets.

5. Discussion and Conclusion

We have investigated the properties of an extensive dataset of magnetosheath jets ($N = 8,499$) using MMS and classified them in different categories based on local magnetosheath measurements. The characteristics

of the different classes correspond to plasma originating from the different values of the angle (θ_{Bn}) between the IMF and the bow shock's normal vector. The general properties found were in agreement with earlier studies. In particular, our data set contains jets with an average duration of ~ 30 s, similar to what has been reported in other studies (Archer & Horbury, 2013; Němeček et al., 1998; Plaschke et al., 2013; Savin et al., 2012). Their dynamic pressure enhancement was found to be in most cases due to both velocity and density enhancement (Amata et al., 2011; Archer & Horbury, 2013; Karlsson et al., 2015; Plaschke et al., 2013). There was no clear case exhibiting a velocity decrease compared to the background magnetosheath, while for all the jets, velocity appears to always be smaller than the associated solar wind measurements. Finally, on average, most of the jets that can be appropriately normalized, have a lower temperature compared to their background. This is in principle expected for a flow that has been less heated and decelerated from the bow shock interaction as shown in previous studies (Amata et al., 2011; Archer et al., 2012; Hietala et al., 2012; Plaschke et al., 2013, 2018; Savin et al., 2008). We have additionally made a number of new observations that are discussed in the following subsections.

5.1. Quasi-Parallel and Quasi-Perpendicular Jets

The results of this study show that quasi-parallel jets are considerably more frequent than quasi-perpendicular jets. Specifically, similar to recent results (Vuorinen et al., 2019), they were found to occur $\sim 5\text{--}10$ times more frequently than quasi-perpendicular jets. On average they have a dynamic pressure around 3.5 nPa, with the majority of them exhibiting both a density and a velocity increase. Their density increase shows a significant correlation with the absolute magnetic field increase ($\rho_{Sp} = 0.5 \pm 0.2$) indicating a possible association of at least a subset of them to SLAMS. A moderate anticorrelation was found between the maximum velocity difference (ΔV_{max}) and the minimum temperature difference (ΔT_{min}). This could be interpreted as a relatively weak support of the bow shock ripple mechanism. Furthermore, the high magnetic field values and variance found could indicate possible wave activity that may contribute to their properties. Finally, most of the quasi-parallel jets are earthward with very high velocities, making them very interesting candidates to investigate phenomena such as jet-triggered magnetopause reconnection or other magnetosphere coupling phenomena.

Quasi-perpendicular jets have a much smaller dynamic pressure than the rest of the classes and their dynamic pressure is mainly due to a velocity increase rather than a density enhancement. Their duration is significantly smaller (median: 4.5 s per jet) and their total integrated dynamic pressure is more than an order of magnitude lower than the corresponding values of the other jet types. While their existence is clear according to the criterion used, their importance regarding magnetospheric influence is to be questioned.

Their properties, when compared to Qpar jets, suggest that either a different mechanism or a smaller scale version of Qpar generation mechanism causes their generation. The density differences can be, in principle, attributed to the absence of SLAMS that are believed to occur only in the ion foreshock generated under quasi-parallel bow shock. On the other hand, we hypothesize that their low velocities compared to the other classes could be the result of one or more of the following effects. The jet criterion used (Equation 1) is fulfilled more easily during low dynamic pressure conditions compared to high dynamic pressure ones. As a result, there might be an observational bias causing MMS to observe primarily jets that occur under low-velocity solar wind conditions. Second, there might be a link between the actual solar wind conditions and the IMF orientation, in which slower solar wind flow could be attributed to IMF conditions where B_y and B_z components are more dominant. Finally, assuming that ripples in the quasi-perpendicular bow shock (Johlander et al., 2016) are related to the jets generation mechanism, maybe the smaller amplitude and scales of these ripples can affect the jet properties. Specifically, the smaller amplitude of Qperp ripples can create a geometry in which the Qperp jet undergoes a larger breaking compared to the case of the sharper (more inclined) transitions of the ripples associated with Qpar jets. The different scales could also contribute to the short duration of the Qperp jets. The smaller scale ripples would benefit the formation of smaller flow structure than larger ones regarding their tangential size. In turn, when these flows meet MMS under some random angle, their measured duration would be significantly smaller.

To investigate the possibility of an observational bias, we examine the distributions of the solar wind velocities associated with and without jets. We find that indeed, on average the associated solar wind velocities are much higher for the quasi-parallel jets ($\langle V_{SW,||,Jets} \rangle \approx 495$ km/s) than for the quasi-perpendicular jets ($\langle V_{SW,\perp,Jets} \rangle \approx 400$ km/s). The standard deviations were found to be $\sigma_{||,Jets} = 96$ km/s and $\sigma_{\perp,Jets} = 46$ km/s, respectively. To calculate the total solar wind distribution, we used 11 months containing long

periods of magnetosheath and jet observations and calculated the average velocity. These months are: October–December 2015 to January, February, November, and December 2016 to January, February, and December 2017 and January 2019, and contained 87% of the jets. The separation between quasi-parallel and quasi-perpendicular was done based on the cone angle being lower or higher than 45°. When observing the total solar wind distribution, solar wind velocities associated with the Qperp bow shock ($\langle V_{SW,\perp} \rangle \approx 421$ km/s) have a smaller difference to the solar wind velocities associated with Qpar bow shock ($\langle V_{SW,\parallel} \rangle \approx 444$ km/s). The standard deviation are found to be $\sigma_{\parallel} = 100$ km/s and $\sigma_{\perp} = 101$ km/s, respectively. As a result, while the difference of the solar wind conditions associated to jets is around ~ 100 km/s, for the solar wind, it is only ~ 20 km/s. It should be noted that, the difference between the Qpar and Qperp solar wind is smaller than 1 standard deviation. Therefore, it is statistically unlikely that it is the effect contributing the most.

From the discussion above, we can conclude that all four effects (absence of SLAMS, observational bias, differences in SW, smaller scale ripples) could in principle take place and contribute to the differences that were observed between the jet properties of Qpar and Qperp jets.

The distance from the bow shock appears to be different for quasi-parallel and quasi-perpendicular jets, with Qpar jets occurring on average closer to the bow shock than Qperp jets. It should be noted, that this result might be artificial since (as discussed above) Qperp jets are found more frequently during low solar wind dynamic pressure conditions, which affects the positions of the bow shock and the magnetopause. As a result, when MMS measures a Qperp jet it will be further away from the bow shock and closer to the magnetopause than a Qpar jet found in the same position. To quantify this effect, we used the average conditions found in the solar wind when Qpar and Qperp jets were observed and derived a model for the magnetopause and the bow shock. It was found that the average standoff distance for the bow shock is $R_{0,BS,\parallel} = 14.8 R_E$ for the Qpar jets and $R_{0,BS,\perp} = 15.3 R_E$ for the Qperp jets. This difference can explain Figure 5. This was expected since in Figure 6, it was already shown that the average position of MMS for both classes is the same. Furthermore, by performing the same procedure for the magnetopause standoff distance, it was found that the average standoff distance is $R_{0,MP,\parallel} = 10.0 R_E$ for the Qpar jets and $R_{0,MP,\perp} = 10.9 R_E$ for the Qperp jets. Once more, this can explain the results shown regarding the magnetopause distance in Figure 6. It should be noted that modeling the bow shock under the typical Qperp SW conditions (very low dynamic pressure) is problematic since in such cases, BS models may overestimate the bow shock distance (Dmitriev et al., 2003). While currently we can compare the position of jets and justify the observed distributions, we cannot draw strong conclusions regarding the relative position of the classes. To do that, a normalization over the magnetosheath regions covered by MMS is required. However, at this point the classification code has been only applied for the jet measurements. Therefore, classified (Qpar and Qperp) magnetosheath observations are not yet available.

It should, however, be noted that while possibly affected by modeling issues, the Qperp jets are indeed found closer to the magnetopause and further away from the bow shock as shown in Figures 5 and 6. While at this point a conclusion regarding their nature cannot be drawn, it is possible that Qperp jets are connected to either small scale bow shock ripples or to flux transfer events (FTEs) that as reported in other studies (Archer & Horbury, 2013) have similar characteristics to Qperp jets shown in this work. While as mentioned above the bow shock ripple mechanism is consistent with our observations, some Qperp jets exhibit properties similar to FTEs. This include density decrease ($\sim 20\%$ of Qperp jets), Alfvénic velocities and southward IMF ($\sim 50\%$ of Qperp jets). As a result, it is possible that the subset of Qperp jets include more than one distinct population with possibly different origin. A possible connection to FTEs is planned to be investigated in more detail in the near future.

Finally, Qperp jets have a velocity increase that is on average equally distributed between each velocity component (Figure 9) and more importantly, velocities of the Qperp jets seem to have a different angle compared to the background flow as shown in Figure 10. This result could mean several things. One possibility would be that the observed subset of Qperp jets originating from low-velocity solar wind can have a specific, predetermined velocity orientation. On the other hand, Qpar jets may also originate from a particularly high-velocity solar wind subset which has another distinct, yet different, velocity orientation. Another possible explanation is that Qperp jets have traveled a longer distance in the magnetosheath region compared to Qpar jet (see Figure 5) which could cause the Qperp jet to have a less distinct difference compared to the background magnetosheath flow.

Qpar and Qperp jets exhibit differences regarding their beta values and how magnetic and thermal pressure contribute to their properties. While a higher β is found in the Qpar jets, when subtracting the contribution of the background magnetosheath, another picture arises. Qpar jets have $\Delta\beta_{mean} < 0$, which means that the magnetic pressure is more important for the jets than for the surrounding magnetosheath. In Qperp jets, however, the jet has a $\Delta\beta_{mean} \sim 0$. Specifically, while the overall region (magnetosheath) is basically dominated in both cases by gas dynamics ($\beta_{mean} > 1$), the Qpar jets are maybe controlled relatively more by magnetic pressure and the Qperp jets are governed slightly more by thermal pressure.

These changes in β parameter can be interpreted via three different mechanisms. First of all, SLAMS originating from the ion foreshock increase the magnetic field of Qpar jets and create an initial increase in the magnetic pressure compared to the Qperp cases where SLAMS are absent. Second, the background magnetosheath regions have differences in density, temperature, and possibly magnetic field, which could contribute to different results both in their total β parameter but also when subtracting the background ($\Delta\beta$). Finally, If we assume that Qperp jets indeed travel longer distances from the bow shock than Qpar jets, the differences in β might provide insight regarding the fate of the jets as they travel in the magnetosheath. Qperp jets are created further away and may have reached a later stage of their existence in which the magnetosheath background flow and the jet are guided equally by the gas dynamics and the background magnetic field. In this case, the weaker Qperp jets are maybe seen in a later stage of their magnetosheath propagation in which their already weak properties make them relatively insignificant to the magnetospheric environment.

5.2. Quasi-Parallel and Boundary Jets

As for the boundary jets, we did not find any significant differences in their properties compared to Qpar jets, indicating a very similar phenomenon. Although some differences can be observed between the two classes, almost all of them can be attributed to the different properties of the background magnetosheath before and after the jet. Specifically, for the boundary jets, by definition, the plasma surrounding them is of both Qpar and Qperp nature. Some authors have speculated that maybe boundary jets are driven primarily by magnetic field tension forces and therefore point to a different origin than the rest of the classes (Archer et al., 2012; Karlsson et al., 2018). However, our results clearly show, both the magnetic field components (Figure 5) and the magnetic field rotation angles (see Figure 10) being very similar to the quasi-parallel jets. Also, all their basic properties are almost identical. Their dynamic pressure and its components have very similar distributions and average values to these of Qpar jets (see Figure 4). The temperature and the magnetic field profiles along with their distance from bow shock are also alike (see Figures 5 and 7). Moreover, the correlations between the different quantities were very similar to the ones found in Qpar jets.

We, therefore, suggest that Qpar and boundary jets form a superset of jets with very similar properties and possibly the same origin. It is unlikely that different physical mechanisms may generate two subsets of jets with so similar statistical properties. One of the things that was not tested, however, is how frequent these jets occur compared to how often we exhibit a switch between Qpar and Qperp magnetosheath. A detailed analysis of that could point out a frequency difference if any.

To summarize, our results suggest that the quasi-parallel and the boundary jets are the classes connected to jet-related phenomena, such as the throat aurora (Han et al., 2017; Wang et al., 2018), magnetopause reconnection (Hietala et al., 2018), and possibly the radiation belts (Turner et al., 2012; Xiang et al., 2016). Finally, both Qpar and boundary jets exhibit high earthward velocities and duration, making them important to investigate magnetosphere coupling phenomena and geoeffective properties.

5.3. Encapsulated Jets

From the observations of the encapsulated jets, we can infer that there are at least two distinct subgroups of jets that are perhaps associated to a different formation mechanism.

The first ones are those that exhibit a positive V_x or that have an extremely small velocity, $|V_x| < 20$ km/s (Figure 9, top left). These rare cases (7/57) could be the result of a plasma reflection from the magnetopause (e.g., Shue et al., 2009). This picture is also consistent with the general trend that encapsulated jets are found closer to the magnetopause than the rest of the jets and could also explain why some of the jets have positive V_x since these reflected flows could in principle point to any direction when measured by MMS at any point of their lifetime.

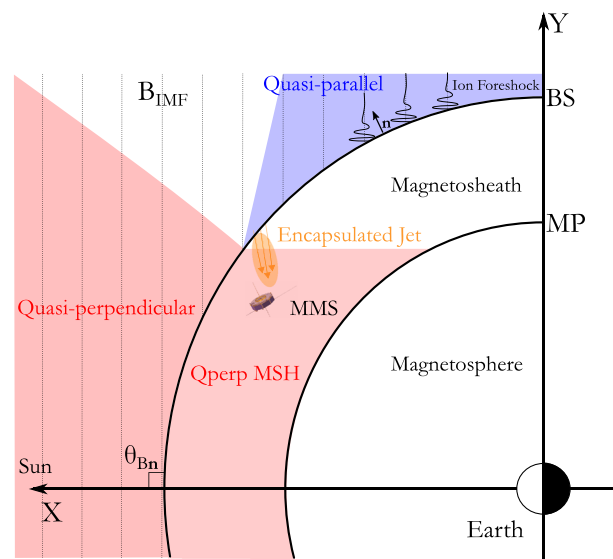


Figure 13. Visualization of encapsulated jet generation model. We assume a purely y component IMF which creates a large region of quasi-perpendicular angles around the subsolar point while the flanks are of quasi-parallel nature. The formation of the jet is done at the flanks of bow shock where ion foreshock is generated. Sequentially, MMS measures the jet traveling from the flanks toward the subsolar point, while the surrounding plasma is characterized by a constant flow originating from the quasi-perpendicular bow shock (red shaded area).

For the encapsulated jets that have a strong enough negative V_x (50/57), a possible scenario is that they are associated with a rotation of the IMF, generating a Qpar and a Qperp plasma environment sequentially. The jet is created in the quasi-parallel plasma environment, having a higher velocity, it gradually overtakes the quasi-perpendicular plasma allowing the formation of a region of Qpar plasma “encapsulated” within the Qperp magnetosheath plasma to be measured by MMS. Another explanation of the encapsulated jets’ statistical properties is that some of them are FTE events, connected to reconnection events occurring at the magnetopause. Structures with similar properties have been suggested to be FTEs (e.g., Bosqued et al., 2001; Petrinec et al., 2020; Phan et al., 2004) and it is possible that part of their set corresponds to such events. This could also explain the strong velocity components in the z and y directions that could result from the outflow region of such events.

Another possible explanation which we propose as the main hypothesis is that the majority of encapsulated jets are a subset of quasi-parallel jets, created at the flanks of the bow shock. This picture provides a direct explanation to the similarities that are generally found between Qpar and encapsulated jets (high velocity increase, low temperature anisotropy, distinct high-energy ion population, etc.). After investigating the associated solar wind conditions it was found that encapsulated jets appear when the IMF is dominated by a y component. This would result in a quasi-perpendicular bow shock close to the subsolar region of the magnetosheath. At the same time, an ion foreshock is formed in the flanks allowing the same effects that apply to Qpar jets to take place. This picture allows a mechanism similarly described to the bow shock ripple mechanism (Hietala & Plaschke, 2013; Hietala et al., 2009) to generate jets. We hypothesize that the orientation of the normal vector (\hat{n}) close to the flanks can deflect the downstream flow into a higher yz velocity component. Then one can speculate that other effects (e.g., local magnetic field deformation, slingshot effects) cause a dominant yz velocity component to be achieved. Finally, the definition we used for encapsulated jets, to be Qpar plasma surrounded by Qperp, creates an observational bias, since in the case that encapsulated jets remain in quasi-parallel environment, they would simply be classified as Qpar jets.

As a result, we believe that encapsulated jets are quasi-parallel jets generated at the flanks, that travel a long distance and are finally measured by MMS in quasi-perpendicular background magnetosheath. This hypothesis is illustrated in Figure 13.

The presented hypothesis also explains how a few encapsulated jets exhibit velocities higher than the upstream solar wind conditions associated to them. First, we have an error at the propagation of solar wind measurements to the bow shock. The data we are using are propagated to the bow shock nose and as a result,

there is a time lag error for the solar wind that arrives at the flanks of the bow shock. Second, such a jet, originating from the flanks of the bow shock, would take a long time to reach the observation point (MMS). As a result, the solar wind measurement association done for each jet is more unreliable for these cases. It should be noted that while this hypothesis could explain the majority of the encapsulated jets, it may not apply for all of them.

None of the presented mechanism can directly explain why encapsulated jets have a density distribution similar to the quasi-perpendicular jets. In Figure 4 we can see that there is little to no density increase within an encapsulated jet. This effect can be seen more clearly when calculating the difference of the mean density for the jet ($\Delta n = \langle n \rangle_{jet} - \langle n \rangle_{5min}$). Doing so we find that on average there is a density decrease in an encapsulated jet ($\Delta n_{mean} = -1.7 \text{ cm}^{-3}$). This is also supported by the distribution of the relative difference in velocity and density that can be seen in Figure 11 and in Table 4. Here, we see several encapsulated jets showing a density decrease.

One mechanism that can explain the density decrease is if expansion takes place while the jet travels through the magnetosheath region. This could also help to explain the difference of the densities found in Qperp jets that are also found at larger distances from the bow shock. To investigate this hypothesis, we search for correlations between the radial (R) distance from the bow shock origin point, and the difference in maximum density (Δn_{max}). Doing so for the subsolar jets ($n = 289$), it was found that they are moderately anticorrelated, $\rho_{Sp,sub solar} = -0.5 \pm 0.05$. It should be noted that this effect remained when looking at class-specific correlations for the case of subsolar Qpar jets ($\rho_{Sp,sub solar,||} = -0.27$). For the rest of the classes, the sample size of subsolar jets was too small to derive any meaningful results. These results could possibly be interpreted as a weak indication of expansion taking place while the jets travel in the magnetosheath region, although for drawing any stronger conclusions more in-depth analysis is required.

Another possibility could be that a diffusion process due to magnetic reconnection or Kelvin-Helmholtz instabilities at the boundary between the jet and the background flow occurs, reducing the density of the jet as it travels in the magnetosheath.

To summarize, the encapsulated jets are found on average further away from the bow shock, they have on average a very large velocity in the yz plane while they usually exhibit a density drop. Their exact nature still needs to be determined. If their origin is associated to the bow shock and not other magnetospheric related events, they can provide vital information regarding the evolution of the jet since we hypothesize that they are flows that while having a high velocity they have undergone an expansion that lowers their density compared to Qpar jets. As a result, such a jet, if created at the flanks of the bow shock, it could create a very interesting case study to investigate the dynamic evolution of its properties from its formation at the bow shock until its observation. However, a possible connection to FTEs could also explain such observations since these jets are occurring close to the magnetopause as shown in Figure 7. A more systematic analysis of these events is required in order to determine the exact nature of this subset of jets.

5.4. Generation Mechanisms of Jets

As mentioned in the previous subsections, the bow shock ripple mechanism (Hietala & Plaschke, 2013; Hietala et al., 2009) is supported indirectly by Figure 7 where we can see that the difference between the temperature of the jet and the background is negative ($\Delta T < 0$) in Qpar jets, indicating that the jet flow could be less decelerated than the background flow by passing through a bow shock ripple. Furthermore, in Figure 12(b,d), it was shown that there is a moderate correlation between the maximum velocity difference and the minimum temperature difference. However, it is very hard to draw any conclusion since the correlations are not robust enough. Although it seems that jet generation could be related to the ripples of the bow shock, there could be more factors that influence their generation that may or may not be connected to this mechanism. A more direct way to evaluate the bow shock ripple mechanism would be to analyze the jets that appear close to the bow shock and compare with those found closer to the magnetopause. Doing so, one can quantify how well the initial properties of the jets are explained through the ripple mechanism and whether this effect gradually diminishes as the jets travel toward the Earth. For the sake of completeness, we looked at jets close to the subsolar point and to the bow shock and we found that the anticorrelation increases ($\rho_{Sp,sub solar} \approx -0.65 \pm 0.1$). However, more careful analysis is needed to investigate this effect and is planned to be done in future studies.

We find support for the SLAMS-related mechanism (Karlsson et al., 2015) when looking at the differences of maximum magnetic pressure (Figure 8) and most importantly at the correlations shown in Figures 12a and 12c between Δn_{max} and $\Delta |B|_{max}$. We conclude that SLAMS play an important role in contributing to the dynamic pressure enhancement of some of the Qpar jets. This can explain some of the differences in the properties of Qperp jets where SLAMS do not occur since they are a phenomenon typically associated with the quasi-parallel bow shock.

Both the bow shock ripple and SLAMS-associated mechanisms are therefore supported and appear to be key elements of jet formation. However, it could be the case that there are more contributing mechanisms to the formation and composition of jets. As previously discussed, the magnetic field is quite different for each class, while it is persistently correlated to several basic properties of most jets. It is possible that the IMF frozen into the solar wind has a more important impact on the jets than previously thought. The high variance of the magnetic field shown in various jets could indicate instabilities and wave activity that may play a role in establishing the jet properties. We believe that more careful investigation regarding phenomena such as acceleration mechanisms, instabilities, and wave interactions might lead to a more complete answer regarding the origin of the jets.

Finally, there have been several cases where the correlations shown in all the jets disappear when investigating class-specific correlations. This can be interpreted as a validation of the classification, showing that the derived classes indeed represent a very similar yet distinct physical phenomenon. However, it also indicates that, on large-scale statistics that include phenomena of diverse nature, correlation-driven conclusions can be unreliable and require further investigation. With the use of advanced techniques originating from probability and information theory (e.g., mutual information) along with careful classification, sampling, and interpretation, we might in the future be able to derive stronger conclusions regarding the origin and generation of jets.

Appendix A: Classification Thresholds and Stages

For the classification process we use the following physical quantities:

$$\text{Averaged "very high" ion differential energy flux} \quad F_{VH} = \frac{1}{3} \sum_i^{30:32} F_i \quad (\text{A1a})$$

$$\text{Averaged "high" ion differential energy flux} \quad F_H = \frac{1}{3} \sum_i^{27:29} F_i \quad (\text{A1b})$$

$$\text{Averaged "medium" ion differential energy flux} \quad F_M = \frac{1}{5} \sum_i^{18:22} F_i \quad (\text{A1c})$$

$$\text{Summed magnetic field standard deviation} \quad \sigma(\mathbf{B}) = \sum_j^{1:3} \sigma(B_j) \quad (\text{A1d})$$

$$\text{Ion temperature anisotropy} \quad Q = \frac{T_\perp}{T_\parallel} - 1 \quad (\text{A1e})$$

$$\text{Total high-/medium-energy flux ratio} \quad C = \frac{F_{VH} + F_H}{F_M} \quad (\text{A1f})$$

where, i is the energy channel of the ion energy spectrum and j is the component of the magnetic field in GSE coordinates. We choose to not multiply with the energy difference (ΔE) for every bin of the energy flux in order to avoid weighting each flux component differently when averaging over. Very high energy

Table A1
Quantities and Thresholds Used for Each Stage of the Classification Procedure

Stages	Quasi-parallel	Quasi-perpendicular
1, 2	$F_{VH,30} > 2.9 \cdot 10^5$ $F_{H,30} > 4 \cdot 10^5$ $\sigma(\vec{B})_{60} > 14$ $Q_{30} < 0.4$ $C > 0.1$	$F_{VH,30} < 2.6 \cdot 10^5$ $F_{H,30} < 3 \cdot 10^5$ $\sigma(\vec{B})_{60} < 13$ $Q_{30} > 0.45$ $C < 0.075$
3	$F_{VH,0} > 3.0 \cdot 10^5$ $F_{H,0} > 4.1 \cdot 10^5$ $\sigma(\vec{B})_{30} > 14$ $Q_0 < 0.3$	$F_{VH,0} < 2.5 \cdot 10^5$ $F_{H,0} < 2.9 \cdot 10^5$ $\sigma(\vec{B})_{30} < 12$ $Q_0 > 0.35$
4, 5	$F'_{VH,0} > \langle F'_{VH,0} \rangle + \Gamma$ $F'_{H,0} > \langle F'_{H,0} \rangle + \Gamma$ $\sigma(\vec{B})'_{30} > \langle \sigma(\vec{B})'_{30} \rangle + \Gamma$ $Q'_0 < \langle Q'_0 \rangle - \Gamma$	$F'_{VH,0} < \langle F'_{VH,0} \rangle - \Gamma$ $F'_{H,0} < \langle F'_{H,0} \rangle - \Gamma$ $\sigma(\vec{B})'_{30} < \langle \sigma(\vec{B})'_{30} \rangle - \Gamma$ $Q'_0 > \langle Q'_0 \rangle + \Gamma$

Note. Number in the subscript indicates the average time window in seconds used for each quantity. Prime quantities (X') indicate a rescaling of the quantity (minimum-maximum normalization: $(X \in [0,1])$). Average quantities ($\langle X \rangle$), are computed starting from 1 minute before the jet up to 1 min after. Finally, $\Gamma = 0.05$ representing a threshold barrier for the normalized quantities. The differential ion energy flux is given in $(\text{keV}/\text{cm}^3 \cdot \text{s} \cdot \text{sr} \cdot \text{keV})$ and the standard deviation of the magnetic field vector in (nT).

flux represents ions of 16–28 keV, high energy is of 7–12 keV, and medium is between 0.55 and 1.7 keV. More information regarding each energy bin can be found by accessing the MMS file repository (<https://lasp.colorado.edu/mms/sdc/public/about/browse-wrapper/>)

The classification process holds several stages, thresholds, and methods. In principle, the thresholds of each quantity are varied according to the values shown in Table A1. It should be noted that not all the thresholds have to be met in order for a classification to be made. Necessary criteria include F_{VH} , F_H , and $\sigma(\vec{B})$, while the others serve mainly as quality indicators and were used only for the classes of Qpar and Qperp jets. Furthermore, the actual classification is being done by separating the jet into three periods as explained in the main text (prejet, jet, postjet). Then we apply these thresholds and classify each period depending on the class of the majority of the data points. During each stage, we vary the time period of prejet and postjet slightly in order to allow the algorithm to take into consideration the different time scales that can occur for every jet.

A simplified flowchart is shown in Figure A1, while a more detailed one can be found in the supporting information. Figure A1 describes the algorithm after the initial clean up of jets is being done. Jets that are found very close to a bow shock crossing or that contain missing data within their prejet/postjet time are not included in the classification algorithm.

As shown in Figure A1, in Stage 1 the jet is classified without any iterative process and by using the thresholds found in Table A1. If a jet does not get classified into one of the main classes, it is moved to Stage 2. In this stage, the algorithm varies the prejet/postjet time for a number of tries to take under consideration possible differences between each jet. There are two kinds of variations that we utilize. First, we change the position of the prejet and postjet periods to be further away from the jet. Then, we slightly increase the period of time that is initialized as described in Equation 5. The next stages take the remaining unclassified jets and change the time average window along with the thresholds (Table A1) while again varying the prejet/postjet times. At this point, the routine finalizes the Qpar and Qperp classes that are shown in Table 3. Moving on to Stage 4, the algorithm identifies potential boundary and encapsulated jets by normalizing the data and using relative thresholds for the classification. The last stage removes one criterion (F_H) in order

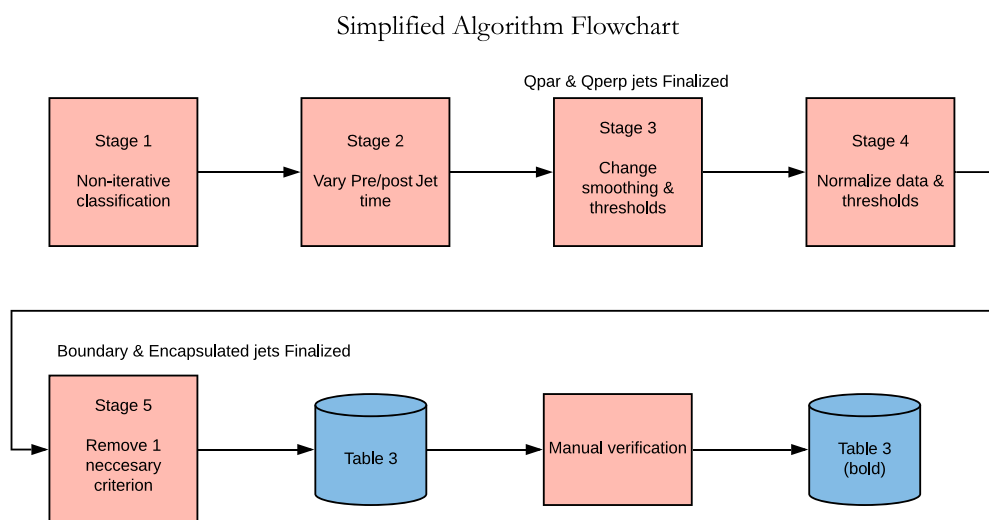


Figure A1. Simplified flowchart of the classification algorithm utilized to generate the data set shown in Table 3.

to allow more jets to be classified to increase the sample size. This stages finalizes the nonemphasized list shown in Table 3. The last step is to manually verify the cases and determine if certain misclassifications occurred, this results in the emphasized (bold) cases shown in Table 3, that are called “final cases.” More information regarding the exact procedure can be found in the supporting information.

Appendix B: Verification Procedure—Fine Parameter Searching

In order to verify the accuracy of the classification scheme, we created a test set of 180 jets (identified by visual inspection) that represent the four main classes as shown in Table 2, or that has been categorized as “unclassified.” This set has been thoroughly checked by visual inspection in order to represent a characteristic sample of the desired classes that we are looking to classify.

To create an initial classification scheme, some coarse threshold values and techniques are implemented which we evaluated using the manually derived test set in order to quantify the accuracy and the misclassification ratio of the code. The first accuracy results can be seen in Table B1.

Accuracy is defined as the percentage of correct classifications. Misclassification is defined as the percentage of classifications that were incorrectly classified to another main class. For example, if a Qpar jet (Class 1) was classified as unknown (Class 0), the accuracy is reduced but the misclassification rate does not increase. On the other hand, if it had been classified as one of the main classes (e.g., boundary (Class 3)) then the misclassification percentage would increase accordingly.

Based on these results, we adjusted the thresholds several times, slightly changed the procedure, and introduced one more stage. Then adjustments were made until a maximum value of accuracy and a minimum value of misclassifications were achieved. The final result of the classification scheme regarding its accuracy can be seen in Table B2.

Table B1
Initial Accuracy Before Fine Parameter Searching

Stage	Q-Par		Q-Perp		Bound.		Encaps.		Unknown
	Acc.	Mis.	Acc.	Mis.	Acc.	Mis.	Acc.	Mis.	Mis.
1	94.7	0	36.4	0	10.8	0	4	4	0
2	94.7	0	39.4	0	10.8	0	20	4	0
3	94.7	0	84.9	0	10.8	0	20	4	11.9
4	94.7	2.6	84.9	3.1	89.2	0	80	4	45.3

Table B2
Final Accuracy After Fine Parameter Searching and Last Modifications

Stage	Q-Par		Q-Perp		Boundary		Encapsulated		Unknown
	Acc.	Mis.	Acc.	Mis.	Acc.	Mis.	Acc.	Mis.	(%)
1	100	0	36.4	0	13.5	0	4	4	0
2	100	0	39.4	0	13.5	0	24	4	2.4
3	100	0	90.9	0	13.5	0	24	4	11.9
4	100	0	90.9	0	89.2	0	76	4	26.2
5	100	0	90.9	0	91.9	0	80	4	26.2

Note. Emphasized text shows the stages that were found to work ideally for each class.

The best sample size and classification accuracy for Qpar and Qperp jets were obtained at Stage 3. As a result, these classes do not get classified in the later stages. Moving on, for the boundary and encapsulated jets due to the complexity of their structure, all 5 stages are used.

The final step was to manually verify the cases that were misclassified from the underrepresented classes (boundary and encapsulated). After doing so, we found no significant difference between the characteristics of the automatically derived database and the manually cleaned one. However, to ensure the scientific value of the results, we validated the data set via manual inspection for the cases that the accuracy results were lower and the number of jets was limited (boundary and encapsulated). This process provided the final data set shown in Table 3, which was then used for the main analysis of this work.

Data Availability Statement

OMNI high-resolution data are available through this site (https://omniweb.gsfc.nasa.gov/form/omni_min.html). The final database of jets can be found in the supporting information or accessed via zenodo data repository (Raptis et al., 2020).

Acknowledgments

We thank the MMS team for providing data and support (<https://lasp.colorado.edu/mms/sdc/public/>). Furthermore, we acknowledge use of NASA/GSFC's Space Physics Data Facility's OMNIWeb service, and OMNI data. This work was supported by Swedish National Space Agency (SNSA grant 90/17).

References

- Amata, E., Savin, S. P., Ambrosino, D., Bogdanova, Y. V., Marcucci, M. F., Romanov, S., & Skalsky, A. (2011). High kinetic energy density jets in the Earth's magnetosheath: A case study. *Planetary and Space Science*, 59(7), 482–494.
- Anderson, B. J., Fuselier, S. A., Gary, S. P., & Denton, R. E. (1994). Magnetic spectral signatures in the Earth's magnetosheath and plasma depletion layer. *Journal of Geophysical Research*, 99(A4), 5877–5891.
- Angelopoulos, V., Kennel, C. F., Coroniti, F. V., Pellat, R., Kivelson, M. G., Walker, R. J., et al. (1994). Statistical characteristics of bursty bulk flow events. *Journal of Geophysical Research*, 99(A11), 21,257–21,280.
- Archer, M. O., Hietala, H., Hartinger, M. D., Plaschke, F., & Angelopoulos, V. (2019). Direct observations of a surface eigenmode of the dayside magnetopause. *Nature Communications*, 10, 615.
- Archer, M. O., & Horbury, T. S. (2013). Magnetosheath dynamic pressure enhancements: Occurrence and typical properties. *Annales Geophysicae*, 31, 319.
- Archer, M. O., Horbury, T. S., & Eastwood, J. P. (2012). Magnetosheath pressure pulses: Generation downstream of the bow shock from solar wind discontinuities. *Journal of Geophysical Research*, 117, A05228. <https://doi.org/10.1029/2011JA017468>
- Behlke, R., André, M., Buchert, S. C., Vaivads, A., Eriksson, A. I., Lucek, E. A., & Balogh, A. (2003). Multi-point electric field measurements of short large-amplitude magnetic structures (SLAMS) at the Earth's quasi-parallel bow shock. *Geophysical Research Letters*, 30(4), 1177. <https://doi.org/10.1029/2002GL015871>
- Bosqued, J. M., Phan, T. D., Dandouras, I., Escoubet, C. P., Rème, H., Balogh, A., et al. (2001). Cluster observations of the high-latitude magnetopause and cusp: initial results from the CIS ion instruments. *Annales Geophysicae*, 19(10/12), 1545–1566. <https://doi.org/10.5194/angeo-19-1545-2001>
- Burch, J., Moore, T., Torbert, R., & Giles, B. (2016). Magnetospheric multiscale overview and science objectives. *Space Science Reviews*, 199(1–4), 5–21.
- Case, N., & Wild, J. (2012). A statistical comparison of solar wind propagation delays derived from multispacecraft techniques. *Journal of Geophysical Research*, 117, A02101. <https://doi.org/10.1029/2011JA016946>
- Chao, J. K., Wu, D. J., Lin, C.-H., Yang, Y.-H., Wang, X. Y., Kessel, M., et al. (2002). Models for the size and shape of the Earth's magnetopause and bow shock. *Cospar Colloquia series*, 12, 127–135.
- Chen, S.-H., Kivelson, M. G., Gosling, J. T., Walker, R. J., & Lazarus, A. J. (1993). Anomalous aspects of magnetosheath flow and of the shape and oscillations of the magnetopause during an interval of strongly northward interplanetary magnetic field. *Journal of Geophysical Research*, 98(A4), 5727–5742.
- Dmitriev, A. V., Chao, J. K., & Wu, D. J. (2003). Comparative study of bow shock models using wind and geotail observations. *Journal of Geophysical Research*, 108(A12), 1464. <https://doi.org/10.1029/2003JA010027>
- Dmitriev, A. V., & Suvorova, A. V. (2012). Traveling magnetopause distortion related to a large-scale magnetosheath plasma jet: THEMIS and ground-based observations. *Journal of Geophysical Research*, 117, A08217. <https://doi.org/10.1029/2011JA016861>

- Dmitriev, A. V., & Suvorova, A. V. (2015). Large-scale jets in the magnetosheath and plasma penetration across the magnetopause: THEMIS observations. *Journal of Geophysical Research: Space Physics*, 120, 4423–4437. <https://doi.org/10.1002/2014JA020953>
- Edgington, E. S. (2011). Randomization tests. In Lovric, M. (Ed.), *International encyclopedia of statistical science* (pp. 1182–1183). Berlin, Heidelberg: Springer Berlin Heidelberg. https://doi.org/10.1007/978-3-642-04898-2_56
- Formisano, V., & Hedgecock, P. C. (1973). Solar wind interaction with the Earth's magnetic field: 3. On the Earth's bow shock structure. *Journal of Geophysical Research*, 78(19), 3745–3760.
- Fuselier, S. A. (2013). Suprathermal ions upstream and downstream from the Earth's bow shock, *Solar wind sources of magnetospheric ultra low frequency waves pp. 107–119*: American Geophysical Union (AGU). <https://doi.org/10.1029/GM081p0107>
- Fuselier, S. A., Anderson, B. J., Gary, S. P., & Denton, R. E. (1994). Inverse correlations between the ion temperature anisotropy and plasma beta in the Earth's quasi-parallel magnetosheath. *Journal of Geophysical Research*, 99(A8), 14,931–14,936.
- Giacalone, J., & Jokipii, J. R. (2007). Magnetic field amplification by shocks in turbulent fluids. *The Astrophysical Journal Letters*, 663(1), L41.
- Gosling, J. T., Asbridge, J. R., Bame, S. J., Paschmann, G., & Sckopke, N. (1978). Observations of two distinct populations of bow shock ions in the upstream solar wind. *Geophysical Research Letters*, 5(11), 957–960.
- Gunell, H., Wieser, G. S., Mella, M., Maggiolo, R., Nilsson, H., Darrouzet, F., et al. (2014). Waves in high-speed plasmoids in the magnetosheath and at the magnetopause. *Annales Geophysicae*, 32, 991–1009.
- Gutynska, O., Sibeck, D. G., & Omidi, N. (2015). Magnetosheath plasma structures and their relation to foreshock processes. *Journal of Geophysical Research: Space Physics*, 120, 7687–7697. <https://doi.org/10.1002/2014JA020880>
- Han, D.-S., Hietala, H., Chen, X.-C., Nishimura, Y., Lyons, L. R., Liu, J.-J., et al. (2017). Observational properties of dayside throat aurora and implications on the possible generation mechanisms. *Journal of Geophysical Research: Space Physics*, 122, 1853–1870. <https://doi.org/10.1002/2016JA023394>
- Hietala, H., Laitinen, T. V., Andreéová, K., Vainio, R., Vaivads, A., Palmroth, M., et al. (2009). Supermagnetosonic jets behind a collisionless quasiparallel shock. *Physical Review Letters*, 103(24), 245001.
- Hietala, H., Partamies, N., Laitinen, T. V., Clausen, L. B. N., Facskó, G., Vaivads, A., et al. (2012). Supermagnetosonic subsolar magnetosheath jets and their effects: From the solar wind to the ionospheric convection. *Annales Geophysicae*, 30(1), 33–48. <https://doi.org/10.5194/angeo-30-33-2012>
- Hietala, H., Phan, T. D., Angelopoulos, V., Oieroset, M., Archer, M. O., Karlsson, T., & Plaschke, F. (2018). In situ observations of a magnetosheath high-speed jet triggering magnetopause reconnection. *Geophysical Research Letters*, 45, 1732–1740. <https://doi.org/10.1002/2017GL076525>
- Hietala, H., & Plaschke, F. (2013). On the generation of magnetosheath high-speed jets by bow shock ripples. *Journal of Geophysical Research: Space Physics*, 118, 7237–7245. <https://doi.org/10.1002/2013JA019172>
- Johlander, A., Schwartz, S. J., Vaivads, A., Khotyaintsev, Y. V., Gingell, I., Peng, I. B., et al. (2016). Rippled quasiperpendicular shock observed by the magnetospheric multiscale spacecraft. *Physical Review Letters*, 117, 165101. <https://doi.org/10.1103/PhysRevLett.117.165101>
- Karlsson, T., Brenning, N., Nilsson, H., Trotignon, J.-G., Vallières, X., & Facskó, G. (2012). Localized density enhancements in the magnetosheath: Three-dimensional morphology and possible importance for impulsive penetration. *Journal of Geophysical Research*, 117, A03227. <https://doi.org/10.1029/2011JA017059>
- Karlsson, T., Kullen, A., Liljeblad, E., Brenning, N., Nilsson, H., Gunell, H., & Hamrin, M. (2015). On the origin of magnetosheath plasmoids and their relation to magnetosheath jets. *Journal of Geophysical Research: Space Physics*, 120, 7390–7403. <https://doi.org/10.1002/2015JA021487>
- Karlsson, T., Plaschke, F., Hietala, H., Archer, M., Blanco-Cano, X., Kajdic, P., et al. (2018). Investigating the anatomy of magnetosheath jets - MMS observations. *Annales Geophysicae*, 36(2), 655–677. <https://doi.org/10.5194/angeo-36-655-2018>
- King, J., & Papitashvili, N. (2005). Solar wind spatial scales in and comparisons of hourly wind and ACE plasma and magnetic field data. *Journal of Geophysical Research*, 110, A02104. <https://doi.org/10.1029/2004JA010649>
- Lavraud, B., Borovsky, J., Ridley, A., Pogue, E., Thomsen, M., Rème, H., et al. (2007). Strong bulk plasma acceleration in earth's magnetosheath: A magnetic slingshot effect? *Geophysical Research Letters*, 34, L14102. <https://doi.org/10.1029/2007GL030024>
- Lin, Y., Swift, D., & Lee, L. (1996). Simulation of pressure pulses in the bow shock and magnetosheath driven by variations in interplanetary magnetic field direction. *Journal of Geophysical Research*, 101(A12), 27,251–27,269.
- Luhmann, J., Russell, C., & Elphic, R. (1986). Spatial distributions of magnetic field fluctuations in the dayside magnetosheath. *Journal of Geophysical Research*, 91(A2), 1711–1715.
- Mailyan, B., Munteanu, C., & Haaland, S. (2008). What is the best method to calculate the solar wind propagation delay? *Annales Geophysicae*, 26, 2383–2394.
- Merka, J., Szabo, A., Narock, T., King, J., Paularena, K., & Richardson, J. (2003). A comparison of IMP 8 observed bow shock positions with model predictions. *Journal of Geophysical Research*, 108(A2), 1077. <https://doi.org/10.1029/2002JA009384>
- Myers, J. L., Well, A. D., & Lorch, R. F. Jr. (2013). *Research design and statistical analysis* (3rd ed.). New York: Routledge. <https://doi.org/10.4324/9780203726631>
- Němcék, Z., Šafránková, J., Přech, L., Sibeck, D., Kokubun, S., & Mukai, T. (1998). Transient flux enhancements in the magnetosheath. *Geophysical Research Letters*, 25(8), 1273–1276.
- Omidi, N., Zhang, H., Sibeck, D., & Turner, D. (2013). Spontaneous hot flow anomalies at quasi-parallel shocks: 2. Hybrid simulations. *Journal of Geophysical Research: Space Physics*, 118, 173–180. <https://doi.org/10.1029/2012JA018099>
- Palmroth, M., Hietala, H., Plaschke, F., Archer, M., Karlsson, T., Blanco-Cano, X., et al. (2018). Magnetosheath jet properties and evolution as determined by a global hybrid-Vlasov simulation. *Annales Geophysicae*, 36, 1171–1182.
- Petrinec, S. (2013). On the magnetic field configuration of the magnetosheath. *Terrestrial, Atmospheric and Oceanic Sciences*, 24, 265. [https://doi.org/10.3319/TAO.2012.10.17.02\(SEC\)](https://doi.org/10.3319/TAO.2012.10.17.02(SEC))
- Petrinec, S. M., Burch, J. L., Chandler, M., Farrugia, C. J., Fuselier, S. A., Giles, B. L., et al. (2020). Characteristics of minor ions and electrons in flux transfer events observed by the magnetospheric multiscale mission. *Journal of Geophysical Research: Space Physics*, 125, e2020JA027778. <https://doi.org/10.1029/2020JA027778>
- Phan, T. D., Dunlop, M. W., Paschmann, G., Klecker, B., Bosqued, J. M., Rème, H., et al. (2004). Cluster observations of continuous reconnection at the magnetopause under steady interplanetary magnetic field conditions. *Annales Geophysicae*, 22(7), 2355–2367. <https://doi.org/10.5194/angeo-22-2355-2004>
- Plaschke, F., & Glassmeier, K.-H. (2011). Properties of standing Kruskal-Schwarzschild-modes at the magnetopause. *Annales Geophysicae*, 29, 1793–1807.
- Plaschke, F., & Hietala, H. (2018). Plasma flow patterns in and around magnetosheath jets. *Annales Geophysicae*, 36, 695–703.

- Plaschke, F., Hietala, H., & Angelopoulos, V. (2013). Anti-sunward high-speed jets in the subsolar magnetosheath. *Annales Geophysicae*, 31, 1877–1889.
- Plaschke, F., Hietala, H., Archer, M., Blanco-Cano, X., Kajdič, P., Karlsson, T., et al. (2018). Jets downstream of collisionless shocks. *Space Science Reviews*, 214(5), 81.
- Pollock, C., Moore, T., Jacques, A., Burch, J., Giese, U., Saito, Y., et al. (2016). Fast plasma investigation for magnetospheric multiscale. *Space Science Reviews*, 199(1–4), 331–406.
- Raptis, S., Karlsson, T., Plaschke, F., Kullen, A., & Lindqvist, P.-A. (2020). Magnetosheath Jets MMS (5/2015 - 6/2019) [Data set]. *Journal of Geophysical Research: Space Physics*. Zenodo. <https://doi.org/10.5281/zenodo.3739553>
- Retinó, A., Sundkvist, D., Vaivads, A., Mozer, F., André, M., & Owen, C. (2007). In situ evidence of magnetic reconnection in turbulent plasma. *Nature Physics*, 3(4), 235.
- Russell, C. T., Anderson, B. J., Baumjohann, W., Bromund, K. R., Dearborn, D., Fischer, D., et al. (2016). The magnetospheric multiscale magnetometers. *Space Science Reviews*, 199(1–4), 189–256.
- Savin, S., Amata, E., Zelenyi, L., Budaev, V., Consolini, G., Treumann, R., et al. (2008). High energy jets in the Earth's magnetosheath: Implications for plasma dynamics and anomalous transport. *JETP Letters*, 87(11), 593–599.
- Savin, S., Amata, E., Zelenyi, L., Lutsenko, V., Safrankova, J., Nemecek, Z., et al. (2012). Super fast plasma streams as drivers of transient and anomalous magnetospheric dynamics. *Annales Geophysicae*, 30(1), 1–7.
- Schwartz, S. J., & Burgess, D. (1991). Quasi-parallel shocks: A patchwork of three-dimensional structures. *Geophysical Research Letters*, 18(3), 373–376.
- Schwartz, S. J., Burgess, D., Wilkinson, W. P., Kessel, R. L., Dunlop, M., & Lühr, H. (1992). Observations of short large-amplitude magnetic structures at a quasi-parallel shock. *Journal of Geophysical Research*, 97(A4), 4209–4227.
- Shue, J.-H., Chao, J.-K., Song, P., McFadden, J. P., Suvorova, A., Angelopoulos, V., et al. (2009). Anomalous magnetosheath flows and distorted subsolar magnetopause for radial interplanetary magnetic fields. *Geophysical Research Letters*, 36, L18112. <https://doi.org/10.1029/2009GL039842>
- Stone, E. C., Frandsen, A., Mewaldt, R., Christian, E., Margolies, D., Ormes, J., & Snow, F. (1998). The advanced composition explorer. *Space Science Reviews*, 86(1–4), 1–22.
- Turc, L., Fontaine, D., Savoini, P., Hietala, H., & Kilpua, E. K. J. (2013). A comparison of bow shock models with cluster observations during low Alfvén Mach number magnetic clouds. *Annales Geophysicae*, 31(6), 1011–1019. <https://doi.org/10.5194/angeo-31-1011-2013>
- Turner, D. L., Shprits, Y., Hartinger, M., & Angelopoulos, V. (2012). Explaining sudden losses of outer radiation belt electrons during geomagnetic storms. *Nature Physics*, 8(3), 208.
- Vuorinen, L., Hietala, H., & Plaschke, F. (2019). Jets in the magnetosheath: IMF control of where they occur. *Annales Geophysicae*, 37, 689–697.
- Wang, B., Nishimura, Y., Hietala, H., Lyons, L., Angelopoulos, V., Plaschke, F., et al. (2018). Impacts of magnetosheath high-speed jets on the magnetosphere and ionosphere measured by optical imaging and satellite observations. *Journal of Geophysical Research: Space Physics*, 123, 4879–4894. <https://doi.org/10.1029/2017JA024954>
- Wilson III, L. B. (2016). Low frequency waves at and upstream of collisionless shocks. *Low-frequency waves in space plasmas* (pp. 269–291): AGU.
- Xiang, Z., Ni, B., Zhou, C., Zou, Z., Gu, X., Zhao, Z., et al. (2016). Multi-satellite simultaneous observations of magnetopause and atmospheric losses of radiation belt electrons during an intense solar wind dynamic pressure pulse. *Annales Geophysicae*, 34(LA-UR-15-27237), 493–509.
- Zhang, H., Sibeck, D., Zong, Q.-G., Omidi, N., Turner, D., & Clausen, L. B. N. (2013). Spontaneous hot flow anomalies at quasi-parallel shocks: 1. Observations. *Journal of Geophysical Research: Space Physics*, 118, 3357–3363. <https://doi.org/10.1002/jgra.50376>